Philosophical Magazine, Vol. X, No. X, Month 2006, xxx–xxx

Nano-scale planar field projection of atomic decohesion and slip in crystalline solids. Part I: A crack-tip cohesive zone

SEUNG TAE CHOI and KYUNG-SUK KIM*
Division of Engineering, Brown University, Providence, RI 02912, USA

The field projection method of Hong and Kim (2004) to identify the crack-tip cohesive zone constitutive relations in an isotropic elastic solid is extended to a nano-scale planar field projection of a cohesive crack tip on an interface between two anisotropic solids. This formulation is applicable to the elastic field of a cohesive crack tip on an interface or in a homogeneous material for any combination of anisotropies. This method is based on a new orthogonal eigenfunction expansion of the elastic field around an interfacial cohesive crack, as well as on the effective use of interaction J integrals. The nano-scale planar field projection is applied to characterizing a crack-tip cohesive zone naturally arising in the fields of atomistics. The atomistic fields analysed are obtained from molecular statics simulations of decohesion in a gold single crystal along a $[\bar{1}\bar{1}2]$ direction in a (111) plane, for which the inter-atomic interactions are described by an embedded atom method potential. The field projection provides cohesive traction, interface separation, and the surface-stress gradient caused by the gradual variation of surface formation within the cohesive zone. Therefore, the cohesive traction and surface energy gradient can be measured as functions of the cohesive zone displacements. The introduction of an atomistic hybrid reference configuration for the deformation analysis has made it possible to complete the field projection and to evaluate the energy release rate of decohesion with high precision. The results of the hybrid analyses of the atomistics and continuum show that there is a nano-scale mechanism of decohesion lattice trapping or hardening caused by the characteristics of non-local atomistic deformations near the crack tip. These characteristics are represented by surface relaxation and the development of surface stresses in the cohesive zone.

Keywords: Nano-scale planar field projection, anisotropic elasticity, molecular statics, crack-tip field, cohesive zone, surface stress

---

[*] Corresponding author. Email: Kyung-Suk_Kim@brown.edu

1. Introduction

The energetics of nano-scale fracture, adhesion, and slip processes in crystalline solids are typically characterised by non-local and nonlinear deformation of the process zone surrounded by a non-uniform field of long-range interaction in a low symmetry, i.e. anisotropic, system. Historically, such nano-scale processes have often been analysed in the view of cohesive zone models in the context of field theory [1--8]. As an illustration, figure 1(a) shows the atomic positions near a crack tip on a $\Sigma 27$ grain boundary in gold simulated by the Embedded Atom Method (EAM) [9]. Details of such simulations will be discussed later in the atomistics section. Such atomic decohesion and/or slip processes in nano-scale are to be analysed from the perspective of a continuum cohesive zone model as depicted in figure 1(b). In the cohesive zone model, the surrounding elastic fields in equilibrium with the state of cohesive zone separation represent the non-uniform deformation characteristics of a long-range interaction with external loading agencies, while the cohesive zone constitutive relations epitomise the non-local and nonlinear deformation characteristics involved in such inter-atomic separation processes. A major energy flux from the external loading to the fracture process zone, upon virtual crack growth, is transmitted through the non-uniform deformation field of a long range interaction. Therefore, it is desirable to characterise the deformation field based on the energetic interaction integrals, e.g. interaction J integral [10], between the atomistic deformation fields (figure 1(a)) and the elastic fields of a cohesive zone model (figure 1(b)). Recently, Hong and Kim [11] found that, due to the crack geometry of the near-field boundary, the elastic fields of cohesive zone models can be decomposed into sets of eigenfunction fields, mutually orthogonal to each other for interaction J integrals. The eigenfunction fields form bases for the interaction integrals to characterise atomic decohesion and/or slip processes. Such a characterising scheme of decohesion and/or slip processes through interactions with the eigenfunction fields of a cohesive zone model is called a planar field projection method (FPM). A formulation of the planar FPM for a crack-tip cohesive zone will be developed in this paper (Part I), while another formulation for a dislocation-core cohesive zone will be presented in a sequel paper (Part II). Once the atomic decohesion process is characterised by the planar FPM, the field-theoretical aspects of the cohesive zone model will be particularly useful in studying the energetic stability of fracture, adhesion, and slip processes.

While, in crystalline solids, the far field lattice deformation surrounding a fracture process zone can be analysed by elastic field theories, the discrete and quantum mechanical nature of atomic debonding in the process zone has been effectively modelled with atomistic simulations [12--18]. In atomistic simulations, fracture-process modelling requires simulation techniques that can handle computationally large numbers of atoms with sufficient accuracy. For such reasons, the atomic resolution aspects of fracture processes have been historically modelled by atomic statics, i.e. atomistics, or molecular dynamics simulations with various semi-empirical inter-atomic potentials, employing limited ab initio calculations to enhance the accuracy of the simulations [19]. The inter-atomic potentials used in the fracture studies include multi-body potentials in general [20--22] and EAM potentials for metals [16, 18, 23]. One of the major difficulties in the atomistic simulation of nano-scale fracture processes is creating a reduced representation of the decohesion processes for various modes of separation from the simulation results. Such difficulty stems from the fact that the energetics of atomistic separation processes in the nano-scale is highly non-local and nonlinear. Such non-local and nonlinear behaviours are treated as cohesive zone constitutive relations in a cohesive zone model [5, 6, 8]. The energetic analysis of fracture processes with a cohesive zone model is particularly useful for solving technologically important problems of controlling the various nano-scale mechanisms of the toughening or embrittlement of solids, including nano-scale solid solution toughening, hydrogen embrittlement, and effects of grain-boundary solute segregation [24].

In conventional cohesive zone models, the cohesive zone is typically characterised by the separation of two cohesive surfaces and associated tractions, assuming that the tractions are in direct equilibrium with the stress state in the surrounding elastic body. In such cohesive zone models, tractions between the surrounding elastic body and cohesive zone surfaces are continuous across the cohesive zone. However, in nano-scale atomic decohesion processes, the surface stresses in the cohesive surfaces must be included in the cohesive zone model, and the tractions between the elastic body and cohesive surfaces become discontinuous across the cohesive zone. Thus, the cohesive zone constitutive relations include not only the separations of cohesive surfaces and the associated work-conjugate tractions, but also the cohesive-zone centre line (CCL) displacements and associated work-conjugate surface stresses. The importance of the surface stresses in surface energetics has been well noted by Schiotz and Carlsson [18] and Wu and Wang [25], but it has not been well reflected in cohesive zone models. Furthermore, in conventional cohesive zone models, attention has been focused mainly on finding the surrounding elastic field for a known state of the cohesive zone, i.e. separation or traction distributions used to solve boundary value problems. However, identifying the cohesive zone constitutive relations from the state of the surrounding far field is an inverse problem. A solution procedure for such inverse problems is called the Field Projection Method (FPM). Recently, Hong and Kim [11] have expressed a general form of the elastic fields of a crack tip with a cohesive zone in a homogeneous isotropic material in terms of an eigenfunction expansion of complex functions in the Muskhelishvili formalism [26]. They also showed an effective use of the eigenfunction expansion in an energetically meaningful FPM, providing an inversion method based on interaction J integrals [10]. However, a class of eigenfunctions that corresponds to the surface stresses in the cohesive zone was not included in their formulation. This class of eigenfunctions is important because surface stresses play significant roles in nano-scale fracture processes. The FPM with a complete set of eigenfunctions is considered particularly useful for a multi-scale analysis of fracture processes with atomistic simulations and for the experimental measurement of nano-scale cohesive zone properties, including surface stresses.

Another important aspect of nano-scale fracture processes in crystalline materials is that deformation develops in a low symmetry system. In other words, the elastic properties are anisotropic and the separation or slip processes are concentrated in a limited set of inter-atomic planes. Therefore, the elastic fields surrounding a cohesive zone must be analysed with anisotropic elasticity. A brief background on the mathematical descriptions of anisotropic elastic crack tip fields follows. Eshelby et al. [27], Stroh [28], and Lekhnitskii [29] developed a linear theory of anisotropic elasticity for a generalised two-dimensional deformation, known as the Stroh formalism. Using the Stroh formalism, Suo [30] expressed the asymptotic elastic field of a sharp crack on the interface in an anisotropic bi-material whose near-tip stress field has oscillatory characteristics in general. Suo [30] decomposed the asymptotic crack-tip stress fields in accordance with the eigenvector direction of the interfacial crack tip characteristic equation for mathematical convenience. Subsequently, Qu and Li [31] obtained another eigenfunction expansion of an interfacial crack, of which stress intensity factors degenerate to conventional stress intensity factors as the bi-material elastic properties reduce to those of homogeneous anisotropic materials. In doing so, Qu and Li [31] introduced a new matrix function that plays an important role in representing the oscillatory characteristics of an interfacial crack tip. Later, Beom and Atluri [32] and Ting [33] independently identified expressions of the generalised Dundurs parameters of dissimilar anisotropic materials, which degenerate to conventional Dundurs parameters [34] as the elastic anisotropy is reduced to isotropy. Beom and Atluri [35] later considered the general Hilbert arc problems to obtain a complete eigenfunction expansion of an interfacial crack, which includes the admissible regular fields, supplementing the non-regular field of Qu and Li [31], at the crack tip.

In this paper, a complete set of eigenfunctions for an interfacial cohesive crack tip field in an anisotropic bi-material is provided and the corresponding FPM is also presented. The complete set includes a subset of eigenfunctions corresponding to the elastic fields caused by surface stresses in the cohesive zone. The complete set of eigenfunctions is orthogonalised for interaction J integrals between the conjugate eigenfunctions within the set. The mathematical structure of the formulation is general and is also applicable to cohesive crack tip fields in homogeneous materials, regardless whether the material is anisotropic or isotropic. Interaction J integrals between atomistic deformation fields at the nano-scale and the eigenfunction fields of the mathematical model build up the nano-scale planar FPM for characterising crack tip decohesion and/or slip processes. While the method is applicable to either experimentally measured or atomistically simulated deformation fields, the method is tested to characterise the atomic decohesion processes in gold with deformation fields from EAM simulations. The test results show that the FPM measures the bounds of the surface energy, as well as the anisotropic surface stress of a solid surface, as a function of cohesive zone displacements. In addition, it is found that the field-projection-nominal (FPN) peak strength of the atomic decohesion is substantially lower, e.g. approximately 4 GPa, than the conventionally estimated rigid-separation-nominal (RSN) strength, e.g. approximately 15 GPa, for gold (111) separation. Furthermore, this hybrid method of decohesion analysis revealed that there is a nano-scale mechanism of decohesion lattice trapping, caused by surface stresses, prior to the dislocation emission or crack growth from a sharp crack tip.

The structure of this paper is as follows. In section 2, the configurational balance in a nano-scale crack-tip cohesive zone model is discussed in terms of conservation integrals, including the surface and interface energies and stresses. In section 3, the eigenfunction expansion is carried out to completely describe the elastic fields near an interfacial crack-tip cohesive zone. Then, a J-orthogonal representation of the eigenfunction expansion is made in section 4 to develop the nano-scale FPM in section 5. Subsequently, in section 6, the FPM is applied to the deformation fields near a crack tip on a (111) plane with a prospective crack growth direction of $[\bar{1}\bar{1}2]$, generated by EAM simulations. In section 7, the results of the analysis carried out in section 6 are discussed. Finally, in section 8, some conclusions are provided. In addition, three appendices, A, B, and C, are attached to provide necessary information on the Stroh matrices, a complex-function representation of the anisotropic elastic field of a bi-material interface crack tip, and the orthogonalisation of the interaction J integral and orthogonal polynomials.

Throughout this paper, a lower case bold Latin character represents a three-component column matrix and an upper case bold Latin character represents a three by three matrix. All italic bold characters indicate tensor quantities, while { } applied to a tensor stands for a matrix composed of the Cartesian components of the tensor associated with the Cartesian coordinates x_1, x_2 and x_3, for which the base vectors are represented by $\boldsymbol{e}_j$, $j = 1, 2$ and 3, respectively. The symbol $\mathbf{I}$ stands for the identity matrix. It is remarked that a summation convention is *not* employed in this article. Subscript indices in < > refer to upper material with 1 and lower material with 2. A prime over a function represents the derivative with respect to the associated argument. A tilde over a matrix symbol indicates that the matrix is diagonal; a tilde over a variable designates a normalised variable; a hat over a function symbol represents an auxiliary function; and bars over any characters denote complex conjugates.

2. Configurational Force Balance in a Nano-Scale Crack-Tip Cohesive Zone Model

A schematic of a nano-scale crack-tip cohesive zone model is shown in figure 2, while the coordinates to describe the cohesive zone model are depicted in figure 1(b). The cohesive zone model is composed of two elements: one for a body region (a) and the other for a surface region (b). For the body region, the conventional elastic field description is applicable. Tractions at the boundary between the surface element and the body element along the cohesive zone, $-c \le x \le c$, are denoted as $\boldsymbol{t}^+$ for the upper part and $\boldsymbol{t}^-$ for the lower part of the cohesive zone. The tractions are related to the stress fields at the boundary of the upper body region <1>, $\boldsymbol{\sigma}^+$, as $\boldsymbol{t}^+ = \boldsymbol{\sigma}^+ \cdot \boldsymbol{e}_2$, and at the boundary of the lower body region <2>, $\boldsymbol{\sigma}^-$, as $\boldsymbol{t}^- = \boldsymbol{\sigma}^- \cdot \boldsymbol{e}_2$. Since the two elements are regarded in reversible static equilibrium in this model, the proper conservation integrals can be applied for the configurational force balances. A relevant conservation integral for this geometry is the J integral [36], defined as:

$$J_\Gamma[S] = \int_\Gamma \left\{ \left(\boldsymbol{e}_1 \cdot \boldsymbol{n}\right)\, \varphi\, [sym(\nabla \boldsymbol{u})] - \left(\boldsymbol{e}_1 \cdot \nabla \boldsymbol{u}\right) \cdot \boldsymbol{\sigma} \cdot \boldsymbol{n} \right\} ds\,, \tag{1}$$

where S symbolises an elastic field collectively representing the elastic displacement field, $\boldsymbol{u}$, and the elastic stress field, $\boldsymbol{\sigma}$; the vector $\boldsymbol{n}$ denotes the outward unit normal of the integral path, Γ; and the strain energy density, φ, is a function of the symmetric part of the displacement gradient, $sym(\nabla \boldsymbol{u})$, which is the linear strain. The J integral vanishes for a closed contour that encloses a regular region.

In cohesive zone models, the J integral along a contour, Γ, that starts from the lower crack face and ends at the upper crack face of the body region, has an energy balance relationship defined as

$$J_\Gamma = \left(\gamma_{<1>} + \gamma_{<2>} - \gamma_{<12>}\right), \tag{2}$$

where γ represents the surface energy density of materials <1> or <2> or the interface <12>.

When the contour Γ_0 only encloses the cohesive zone boundary in the body region, the J integral can be expressed as

$$\begin{aligned} J_{\Gamma_0} &= \int_{-c}^{c} \left(\boldsymbol{t}^{+} \cdot \frac{\partial \boldsymbol{u}^{+}}{\partial x_1} - \boldsymbol{t}^{-} \cdot \frac{\partial \boldsymbol{u}^{-}}{\partial x_1} \right) dx_1 \\ &= \int_{-c}^{c} \left[\left(\boldsymbol{t}^{+} - \boldsymbol{t}^{-} \right) \cdot \left\{ \frac{1}{2} \left(\frac{\partial \boldsymbol{u}^{+}}{\partial x_1} + \frac{\partial \boldsymbol{u}^{-}}{\partial x_1} \right) \right\} + \left\{ \frac{1}{2} \left(\boldsymbol{t}^{+} + \boldsymbol{t}^{-} \right) \right\} \cdot \left(\frac{\partial \boldsymbol{u}^{+}}{\partial x_1} - \frac{\partial \boldsymbol{u}^{-}}{\partial x_1} \right) \right] dx_1 \\ &= \int_{-c}^{c} \left(\boldsymbol{\tau} \cdot \frac{\partial \boldsymbol{u}^{a}}{\partial x_1} + \boldsymbol{t}^{a} \cdot \frac{\partial \boldsymbol{\delta}}{\partial x_1} \right) dx_1, \end{aligned} \tag{3}$$

where $\boldsymbol{\tau}$ is the traction jump, $\boldsymbol{t}^{+} - \boldsymbol{t}^{-}$; $\boldsymbol{\delta}$ is the displacement jump, $\boldsymbol{u}^{+} - \boldsymbol{u}^{-}$; $\boldsymbol{t}^{a}$ is the average traction, $(\boldsymbol{t}^{+} + \boldsymbol{t}^{-})/2$; and $\boldsymbol{u}^{a}$ is the average displacement, $(\boldsymbol{u}^{+} + \boldsymbol{u}^{-})/2$. The average displacement is the cohesive-zone centre line (CCL) displacement. In conventional cohesive zone models, $\boldsymbol{\tau}$ vanishes; however, in nano-scale cohesive zone models, the average surface stress, $\boldsymbol{\Sigma}^{a} (= (\boldsymbol{\Sigma}^{+} + \boldsymbol{\Sigma}^{-})/2)$, along the cohesive zone can balance the traction jump as $\boldsymbol{\tau} + \nabla \cdot \boldsymbol{\Sigma}^{a} = \mathbf{0}$, neglecting the second order effect of CCL curvature. For a one-dimensional cohesive zone as shown in figure 2(b), the net force balance of the surface element becomes

$$\int_{-c}^{c} \tau_1 dx_1 = \Sigma_{0<1>} + \Sigma_{0<2>} - \Sigma_{0<12>}, \tag{4}$$

where $\Sigma_{0<\mu>}$ for $\mu = 1, 2$ or 12 means $\Sigma_{11<\mu>}$ on a free surface for surface stresses or on a fully bonded interface for an interface stress. On a free surface, $\gamma = \gamma_0 + \mathbf{\Sigma}_0 : \boldsymbol{\varepsilon}^{s}$ with a surface strain of $\boldsymbol{\varepsilon}^{s}$ [25].

When the elastic field is linear, two independent equilibrium fields, $S[\boldsymbol{\sigma}, \boldsymbol{u}]$ and $\hat{S}[\hat{\boldsymbol{\sigma}}, \hat{\boldsymbol{u}}]$, can be superposed and the interaction J integral, $J_{\Gamma}^{\text{int}}[S, \hat{S}]$ [10], between S and $\hat{S}$ along the path Γ is defined as

$$\begin{aligned} J_{\Gamma}^{\text{int}}[S, \hat{S}] &= J_{\Gamma}[S + \hat{S}] - J_{\Gamma}[S] - J_{\Gamma}[\hat{S}] \\ &= \int_{\Gamma} \left[\left(\boldsymbol{e}_1 \cdot \boldsymbol{n} \right) \left(\boldsymbol{\sigma} : \nabla \hat{\boldsymbol{u}} \right) - \left(\boldsymbol{e}_1 \cdot \nabla \hat{\boldsymbol{u}} \right) \cdot \boldsymbol{\sigma} \cdot \boldsymbol{n} - \left(\boldsymbol{e}_1 \cdot \nabla \boldsymbol{u} \right) \cdot \hat{\boldsymbol{\sigma}} \cdot \boldsymbol{n} \right] ds. \end{aligned} \tag{5}$$

The $J_{\Gamma}[S]$ integral, as well as the interaction integral $J_{\Gamma}^{\text{int}}[S, \hat{S}]$, are path independent among homologous paths that enclose a cohesive zone. Since the interaction J integral provides a way of interrogating an unknown field with a known set of fields, a well characterised set of elastic eigenfunction fields of a crack-tip cohesive zone is developed in the following sections; these functions can be used for such interrogations.

3. Eigenfunction Expansion of Interfacial Cohesive Crack-Tip Elastic Fields

A displacement field, $\boldsymbol{u}$, and the corresponding stress field, $\boldsymbol{\sigma}$, of an anisotropic elastic medium in static equilibrium without a body force in a two-dimensional (x_1, x_2) plane can be expressed in a compact form as [27, 28]

$$\{\boldsymbol{u}\} = 2\,\mathrm{Re}\big[\mathbf{A}\mathbf{f}(z)\big], \tag{6}$$

$$\begin{bmatrix} \{\boldsymbol{e}_1 \cdot \boldsymbol{\sigma}\} \\ \{\boldsymbol{e}_2 \cdot \boldsymbol{\sigma}\} \end{bmatrix} = 2\,\mathrm{Re}\begin{bmatrix} -\mathbf{B}\tilde{\boldsymbol{\lambda}}\mathbf{f}'(z) \\ \mathbf{B}\mathbf{f}'(z) \end{bmatrix}, \tag{7}$$

where $\mathbf{f}(z) \equiv \sum_{j=1}^{3} f_j(z_j)\{\boldsymbol{e}_j\}$ is a column matrix representation of the three analytic functions of the respective complex variables $z_j = x_1 + p_j x_2$; the Stroh eigenvalue, p_j, and the Stroh matrices, $\mathbf{A}$ and $\mathbf{B}$, are defined in appendix A. The matrix $\tilde{\boldsymbol{\lambda}}$ is a diagonal matrix with the components $p_j \delta_{jk}$, where δ_{jk} is the Kronecker delta. The argument z represents z_j for the corresponding *j*'th row of the function matrix $\mathbf{f}(z)$.

An anisotropic bi-material with its interface on the x_1 axis has a traction-free, semi-infinite interfacial crack along $x_1 < -c$ and a cohesive zone on $-c \le x_1 \le c$, as shown in figure 1. The elastic fields around the cohesive zone can be described by the superposition of the non-singular eigenfunctions of sharp-crack-tip elastic fields with respect to $x_1 = -c$ and $x_1 = c$, as Hong and Kim [11] did for a cohesive crack tip field in a homogeneous isotropic solid. In addition, the elastic field caused by the surface stress along the cohesive zone faces must be superposed for nano-scale cohesive crack tip fields; the surface stress appears to be a traction jump between the two faces of the cohesive zone. Based on the eigenfunction expression, (B1) in appendix B, of a sharp-crack-tip elastic field, the column matrix function $\mathbf{f}'(z)$ of the bi-material cohesive crack tip field can be described as

$$\begin{aligned} \mathbf{f}'_{<\mu>}(z) = {} & \frac{1}{2}\mathbf{B}^{-1}_{<\mu>}\big[\mathbf{I} - (-1)^{\mu} i\boldsymbol{\beta}\big]\Big\{\mathbf{Y}\big[(z+c)^{-i\varepsilon}\big]\mathbf{g}(z)\sqrt{z+c} - \mathbf{Y}\big[(z-c)^{-i\varepsilon}\big]\mathbf{h}(z)\sqrt{z-c}\Big\} \\ & + \frac{i}{2}\mathbf{B}^{-1}_{<\mu>}\big[\mathbf{I} - (-1)^{\mu}\boldsymbol{\alpha}\big]\Big[\mathbf{q}(z)\sqrt{z^2 - c^2} + \mathbf{r}(z)\Big], \end{aligned} \tag{8}$$

for $\mu = 1 \text{ or } 2$ referring to materials 1 or 2, respectively. The four analytic matrix functions $\mathbf{g}(z)$, $\mathbf{h}(z)$, $\mathbf{q}(z)$, and $\mathbf{r}(z)$ can be expressed as a series, $\sum_{n=0}^{\infty}\mathbf{G}_n(z)\mathbf{g}_n$, $\sum_{n=0}^{\infty}\mathbf{H}_n(z)\mathbf{h}_n$, $\sum_{n=0}^{\infty}\mathbf{Q}_n(z)\mathbf{q}_n$, and $\sum_{n=0}^{\infty}\mathbf{R}_n(z)\mathbf{r}_n$, for which $\mathbf{G}_n(z)$, $\mathbf{H}_n(z)$, $\mathbf{Q}_n(z)$, and $\mathbf{R}_n(z)$ are real matrix base functions, for example, $\mathbf{G}_n(z) = \bar{\mathbf{G}}_n(z)$, and $\mathbf{g}_n$, $\mathbf{h}_n$, $\mathbf{q}_n$, and $\mathbf{r}_n$ are column matrices of real coefficients. The generalised Dundurs parameter real matrices $\boldsymbol{\alpha}$ and $\boldsymbol{\beta}$, the bi-material oscillatory index ε, and the bi-material real function matrix $\mathbf{Y}\left[\eta(z)\right]$ for an arbitrary function $\eta(z)$ are defined in appendix B for anisotropic bi-materials. It is worth noting that the oscillatory fields near the two ends of the cohesive zone resulting from the eigenfunction expansion given in equation (3) do not give physically unacceptable phenomena because it does not include a term of diverging stress in the eigenfunction expansion.

The decomposition of the function $\mathbf{f}'_{<\mu>}(z)$ into $\mathbf{g}(z)$, $\mathbf{h}(z)$, $\mathbf{q}(z)$, and $\mathbf{r}(z)$ in equation (8) is analogous to that made by Hong and Kim [11] for a cohesive crack tip field in a homogeneous isotropic solid. The function $\mathbf{g}(z)$ is responsible for the traction distribution at the cohesive zone, while the function $\mathbf{h}(z)$ is responsible for the separation variations along the cohesive zone. To take into account the elastic field of the surface energy gradient along the cohesive zone, which was ignored by Hong and Kim [11], the $\mathbf{q}(z)$ function is introduced here. The term $\mathbf{q}(z)$ is important for nano-scale fracture problems; however, it is negligible for large-scale fracture problems in general. Including a regular field near the cohesive zone represented by the function $\mathbf{r}(z)$, for which the corresponding traction along x_1 axis vanishes, the holomorphic function $\mathbf{f}'_{<\mu>}(z)$ in equation (8) constructs a complete set of eigenfunction expansions near a cohesive crack tip on an interface between two anisotropic solids. In the following section, the eigenfunctions are orthogonalised to the orthogonal base functions, $\mathbf{G}_n^o(z)$, $\mathbf{H}_n^o(z)$, $\mathbf{Q}_n^o(z)$, and $\mathbf{R}_n^o(z)$ with respect to the interaction J integral [10]. The eigenfunction expansion based on such base functions is called the J-orthogonal representation.

4. J-Orthogonal Representation of the Cohesive Zone Eigenfunction Expansion

In this section, a set of well characterised eigenfunction fields for a cohesive zone is developed and these eigenfunction fields can also be conveniently used to interrogate other elastic fields with interaction J integrals. In particular, the interaction will be between configurational-work-conjugate sets of eigenfunctions. When the interaction J integral, equation (5), is applied to the contour Γ_0 along the faces of the cohesive zone, the traction and displacement gradient along the cohesive zone are required to evaluate the interaction J integral. The traction along the cohesive zone, equation (7), is expressed explicitly with the eigenfunction expansion in equation (8) as

$$\left\{\boldsymbol{e}_2\cdot\boldsymbol{\sigma}(x_1)\right\}_{<\mu>}=\mathbf{Y}\left[(c+x_1)^{-i\varepsilon}\right]\mathbf{g}(x_1)\sqrt{c+x_1}+(-1)^{\mu}\left[\mathbf{I}-(-1)^{\mu}\boldsymbol{\alpha}\right]\mathbf{q}(x_1)\sqrt{c^2-x_1^2}\ , \tag{9}$$

for $\mu=1$ or 2 referring to materials 1 or 2, respectively; while the displacement gradient along the cohesive zone is given by

$$\begin{aligned}\left\{\boldsymbol{e}_1\cdot\nabla\boldsymbol{u}(x_1)\right\}_{<\mu>}&=\operatorname{Im}\left\{\mathbf{M}_{<\mu>}^{-1}\left[\mathbf{I}-(-1)^{\mu}i\boldsymbol{\beta}\right]\right\}\mathbf{Y}\left[(c+x_1)^{-i\varepsilon}\right]\mathbf{g}(x_1)\sqrt{c+x_1}\\&\quad+(-1)^{\mu}\mathbf{L}_{<\mu>}^{-1}\left[\mathbf{I}-(-1)^{\mu}i\boldsymbol{\beta}\right]\mathbf{Y}\left[(c-x_1)^{-i\varepsilon}e^{\pi\varepsilon}\right]\mathbf{h}(x_1)\sqrt{c-x_1}\\&\quad-(-1)^{\mu}\mathbf{W}_{<\mu>}\left[\mathbf{I}-(-1)^{\mu}\boldsymbol{\alpha}\right]\mathbf{q}(x_1)\sqrt{c^2-x_1^2}+\mathbf{L}_{<\mu>}^{-1}\left[\mathbf{I}-(-1)^{\mu}\boldsymbol{\alpha}\right]\mathbf{r}(x_1),\end{aligned} \tag{10}$$

for $\mu=1$ or 2 referring to materials 1 or 2, respectively. Definitions of the elastic property matrices $\mathbf{M}$, $\mathbf{L}$, and $\mathbf{W}$ used in equation (10) are given in appendices A and B.

Then, by inserting equations (9) and (10) into equation (5), the expression of the interaction J integral is reduced to

$$\begin{aligned}J_{\Gamma_o}^{\text{int}}[S,\hat{S}]&=-\int_{-c}^{c}\left[\!\left[\left\{\boldsymbol{e}_2\cdot\boldsymbol{\sigma}(x_1)\right\}^T\left\{\boldsymbol{e}_1\cdot\nabla\hat{\boldsymbol{u}}(x_1)\right\}+\left\{\boldsymbol{e}_2\cdot\hat{\boldsymbol{\sigma}}(x_1)\right\}^T\left\{\boldsymbol{e}_1\cdot\nabla\boldsymbol{u}(x_1)\right\}\right]\!\right]dx_1\\&=\int_{-c}^{c}\sqrt{c^2-x_1^2}\left\{\mathbf{g}^T(x_1)\mathbf{U}^{-1}\mathbf{Y}\left[\eta_c(x_1)\right]\hat{\mathbf{h}}(x_1)+\hat{\mathbf{g}}^T(x_1)\mathbf{U}^{-1}\mathbf{Y}\left[\eta_c(x_1)\right]\mathbf{h}(x_1)\right\}dx_1\\&\quad+4\int_{-c}^{c}\sqrt{c^2-x_1^2}\left[\mathbf{q}^T(x_1)\left(\mathbf{L}_{<1>}+\mathbf{L}_{<2>}\right)^{-1}\hat{\mathbf{r}}(x_1)+\hat{\mathbf{q}}^T(x_1)\left(\mathbf{L}_{<1>}+\mathbf{L}_{<2>}\right)^{-1}\mathbf{r}(x_1)\right]dx_1,\end{aligned} \tag{11}$$

where the double bracket $[\![\cdots]\!]$ indicates a jump across the cohesive zone; the elastic property matrix , $\mathbf{U}^{-1}$, is defined as $\mathbf{U}^{-1}=\left(\mathbf{L}_{<1>}^{-1}+\mathbf{L}_{<2>}^{-1}\right)\left(\mathbf{I}+\boldsymbol{\beta}^2\right)$; and the function $\eta_c(x_1)=\left[(c-x_1)/(c+x_1)\right]^{-i\varepsilon}\cosh\pi\varepsilon$. In deriving the second equality of equation (11), various identity relationships of equation (B5) in appendix B were used, and only four terms survived among the sixteen interaction pairs between { $\mathbf{g}(z)$, $\mathbf{h}(z)$, $\mathbf{q}(z)$, $\mathbf{r}(z)$ } and { $\hat{\mathbf{g}}(z)$, $\hat{\mathbf{h}}(z)$, $\hat{\mathbf{q}}(z)$, $\hat{\mathbf{r}}(z)$ }. The result shows the distinct configurational-work-conjugate pairs of { $\mathbf{g}(z)$, $\mathbf{h}(z)$ } and { $\mathbf{q}(z)$, $\mathbf{r}(z)$ }. Equation (11) can be further reduced by constructing orthogonal base functions of $\mathbf{g}(z)$, $\mathbf{h}(z)$, $\mathbf{q}(z)$, and $\mathbf{r}(z)$ as $\mathbf{G}_n^o(\tilde{z})=\mathbf{V}^{-T}\tilde{\mathbf{P}}_n(\tilde{z})\mathbf{V}^T$, $\mathbf{H}_n^o(\tilde{z})=\bar{\mathbf{V}}^{-T}\tilde{\mathbf{P}}_n(\tilde{z})\bar{\mathbf{V}}^T$, $\mathbf{Q}_n^o(\tilde{z})=U_n(\tilde{z})\mathbf{I}$, and $\mathbf{R}_n^o(\tilde{z})=U_n(\tilde{z})\mathbf{I}$, where $\tilde{z}$ denotes z/c; $\mathbf{V}$ denotes a Hermitian matrix defined in appendix C; $\tilde{\mathbf{P}}_n(\tilde{z})$ denotes the diagonal matrix functions of normalised Jacobi polynomials with the components $\delta_{jk}\, P_n^{(a_j,\bar{a}_j)}(\tilde{z})\big/\theta_n^{(a_j,\bar{a}_j)}$; $U_n(z) = P_n^{(1/2,1/2)}(z)\big/\theta_n^{(1/2,1/2)}$ denotes the Chebyshev polynomials of the second kind; and $\theta_n^{(a,b)}$ denotes the normalisation factors of the Jacobi polynomial $P_n^{(a,b)}(z)$. The explicit expression of $\theta_n^{(a,b)}$ and the details of the orthogonalisation with Jacobi polynomials for interaction J integrals are provided in appendix C.

With the orthogonal eigenfunctions, the stress function $\mathbf{f}'_{<\mu>}(z)$ is then expressed as

$$\mathbf{f}'_{<\mu>}(z) = \sum_{n=0}^{N} \left\{ \mathscr{G}^{o}_{n<\mu>}(\tilde{z})\mathbf{g}_n + \mathscr{H}^{o}_{n<\mu>}(\tilde{z})\mathbf{h}_n + \mathscr{Q}^{o}_{n<\mu>}(\tilde{z})\mathbf{q}_n + \mathscr{R}^{o}_{n<\mu>}(\tilde{z})\mathbf{r}_n \right\}, \tag{12}$$

where $\mathbf{g}_n$, $\mathbf{h}_n$, $\mathbf{q}_n$, and $\mathbf{r}_n$ are column matrices of real coefficients, and

$$\begin{aligned}
\mathscr{G}^{o}_{n<\mu>}(\tilde{z}) &= \frac{1}{2}\sqrt{\tilde{z}+1}\,\mathbf{B}^{-1}_{<\mu>}\left[\mathbf{I}-(-1)^{\mu} i\boldsymbol{\beta}\right]\mathbf{Y}\left[(\tilde{z}+1)^{-i\varepsilon}\right]\mathbf{G}^{o}_{n}(\tilde{z}),\\
\mathscr{H}^{o}_{n<\mu>}(\tilde{z}) &= -\frac{1}{2}\sqrt{\tilde{z}-1}\,\mathbf{B}^{-1}_{<\mu>}\left[\mathbf{I}-(-1)^{\mu} i\boldsymbol{\beta}\right]\mathbf{Y}\left[(\tilde{z}-1)^{-i\varepsilon}\right]\mathbf{Y}^{-1}\left[\cosh \pi\varepsilon\right]\mathbf{H}^{o}_{n}(\tilde{z}),\\
\mathscr{Q}^{o}_{n<\mu>}(\tilde{z}) &= \frac{i}{2}\sqrt{\tilde{z}^{2}-1}\,\mathbf{B}^{-1}_{<\mu>}\left[\mathbf{I}-(-1)^{\mu}\boldsymbol{\alpha}\right]\mathbf{Q}^{o}_{n}(\tilde{z}),\\
\mathscr{R}^{o}_{n<\mu>}(\tilde{z}) &= \frac{i}{2}\mathbf{B}^{-1}_{<\mu>}\left[\mathbf{I}-(-1)^{\mu}\boldsymbol{\alpha}\right]\mathbf{R}^{o}_{n}(\tilde{z}).
\end{aligned} \tag{13}$$

Expressing the auxiliary field, as well as the actual field of interest, in the same form of eigenfunction expansion, equation (12), and substituting the eigenfunctions into equation (11), the interaction integral, $J^{\mathrm{int}}_{\Gamma_o}[S,\hat{S}]$, is obtained in terms of the coefficients of the eigenfunctions:

$$J^{\mathrm{int}}_{\Gamma_o}[S,\hat{S}] = \frac{\pi c}{2}\sum_{n=0}^{N}\left[\mathbf{g}_n^{T}\mathbf{U}^{-1}\hat{\mathbf{h}}_n + \hat{\mathbf{g}}_n^{T}\mathbf{U}^{-1}\mathbf{h}_n + 4\mathbf{q}_n^{T}\left(\mathbf{L}_{<1>}+\mathbf{L}_{<2>}\right)^{-1}\hat{\mathbf{r}}_n + 4\hat{\mathbf{q}}_n^{T}\left(\mathbf{L}_{<1>}+\mathbf{L}_{<2>}\right)^{-1}\mathbf{r}_n\right]. \tag{14}$$

When the auxiliary field is chosen to be the actual field, the interaction integral becomes twice the value of the J integral. As shown in equation (14), the eigenfunction fields selectively interact with other fields in the interaction J integral. Therefore, the interaction J integrals with the eigenfunctions can be used as filters for the fields to be interrogated. In addition, the interaction J integral is path independent so that the integral can be evaluated at some distance from the cohesive zone. In other words, the cohesive zone characteristics can be assessed using far-field data. The method of assessing local properties with far-field data with an FPM is discussed in the following section.

5. Field Projection Method for a J-Equivalent Crack-Tip Cohesive Zone

In the previous section it was shown that, with the base eigenfunctions, an infinite series of four real column matrices, $\mathbf{g}_n$, $\mathbf{h}_n$, $\mathbf{q}_n$, and $\mathbf{r}_n$, completely determine the field surrounding the cohesive zone in the cohesive zone model. In this section, formulas to determine the four real column matrices with interaction J integrals are provided. The four real column matrices, $\mathbf{g}_n$, $\mathbf{h}_n$, $\mathbf{q}_n$, and $\mathbf{r}_n$, are responsible for cohesive zone tractions, separations, surface stresses, and cohesive-zone centre line (CCL) displacements, respectively. If an auxiliary field of $\hat{S}^{(k)}_{\mathbf{h}_n}$ for which $\hat{\mathbf{h}}_n = \{\boldsymbol{e}_k\}$ (k=1,2,3) and $\hat{\mathbf{g}}_n = \hat{\mathbf{q}}_n = \hat{\mathbf{r}}_n = \mathbf{0}$, i.e. $\hat{\mathbf{f}}'_{<\mu>}(z) = \boldsymbol{\mathcal{H}}^{o}_{n<\mu>}(\tilde{z})\{\boldsymbol{e}_k\}$, is used in equation (14), the interaction J integral is simply expressed as $J^{\text{int}}_{\Gamma_o}[S, \hat{S}^{(k)}_{\mathbf{h}_n}] = (\pi c/2)\mathbf{g}_n^T \mathbf{U}^{-1}\{\boldsymbol{e}_k\}$. Subsequently, this relationship can be easily inverted to become

$$\mathbf{g}_n = \frac{2}{\pi c}\mathbf{U}\left[J^{\text{int}}_{\Gamma}[S, \hat{S}^{(1)}_{\mathbf{h}_n}],\, J^{\text{int}}_{\Gamma}[S, \hat{S}^{(2)}_{\mathbf{h}_n}],\, J^{\text{int}}_{\Gamma}[S, \hat{S}^{(3)}_{\mathbf{h}_n}]\right]^T, \quad n = 1, 2, \cdots, N. \tag{15a}$$

Similarly, with an auxiliary field, $\hat{S}^{(k)}_{\mathbf{g}_n}$, of $\hat{\mathbf{f}}'_{<\mu>}(z) = \boldsymbol{\mathcal{G}}^{o}_{n<\mu>}(\tilde{z})\{\boldsymbol{e}_k\}$ for k=1,2,3,

$$\mathbf{h}_n = \frac{2}{\pi c}\mathbf{U}\left[J^{\text{int}}_{\Gamma}[S, \hat{S}^{(1)}_{\mathbf{g}_n}],\, J^{\text{int}}_{\Gamma}[S, \hat{S}^{(2)}_{\mathbf{g}_n}],\, J^{\text{int}}_{\Gamma}[S, \hat{S}^{(3)}_{\mathbf{g}_n}]\right]^T, \quad n = 1, 2, \cdots, N \tag{15b}$$

is obtained; with an auxiliary field, $\hat{S}^{(k)}_{\mathbf{r}_n}$, of $\hat{\mathbf{f}}'_{<\mu>}(z) = \boldsymbol{\mathcal{R}}^{o}_{n<\mu>}(\tilde{z})\{\boldsymbol{e}_k\}$ for k=1,2,3,

$$\mathbf{q}_n = \frac{1}{2\pi c}\left(\mathbf{L}_{<1>} + \mathbf{L}_{<2>}\right)\left[J^{\text{int}}_{\Gamma}[S, \hat{S}^{(1)}_{\mathbf{r}_n}],\, J^{\text{int}}_{\Gamma}[S, \hat{S}^{(2)}_{\mathbf{r}_n}],\, J^{\text{int}}_{\Gamma}[S, \hat{S}^{(3)}_{\mathbf{r}_n}]\right]^T, \quad n = 1, 2, \cdots, N; \tag{15c}$$

and finally with an auxiliary field, $\hat{S}^{(k)}_{\mathbf{q}_n}$, of $\hat{\mathbf{f}}'_{<\mu>}(z) = \boldsymbol{\mathcal{Q}}^{o}_{n<\mu>}(\tilde{z})\{\boldsymbol{e}_k\}$ for k=1,2,3,

$$\mathbf{r}_n = \frac{1}{2\pi c}\left(\mathbf{L}_{<1>} + \mathbf{L}_{<2>}\right)\left[J^{\text{int}}_{\Gamma}[S, \hat{S}^{(1)}_{\mathbf{q}_n}],\, J^{\text{int}}_{\Gamma}[S, \hat{S}^{(2)}_{\mathbf{q}_n}],\, J^{\text{int}}_{\Gamma}[S, \hat{S}^{(3)}_{\mathbf{q}_n}]\right]^T, \quad n = 1, 2, \cdots, N. \tag{15d}$$

As shown in equations (15a-d), for an arbitrary elastic field of a cohesive zone model, the field near the cohesive zone determined by $\mathbf{g}_n$, $\mathbf{h}_n$, $\mathbf{q}_n$, and $\mathbf{r}_n$ can be assessed by interaction J integrals along a contour Γ at a distance away from the cohesive zone. This is an attractive feature of the FPM for experimental measurements or atomistic simulations of the cohesive zone characteristics. As long as the elastic-field data in a region that encloses the cohesive zone at some distance is available, cohesive zone characteristics can be evaluated. When the FPM is applied to an elastic field that is linearly elastic all the way close to a planar cohesive zone, as shown in figure 1(b) or figure 2, the assessment can achieve an arbitrary accuracy with a large number, *N*, in equations (15a-d). However, when the method is applied to an elastic field that embraces not only a planar cohesive zone but also a non-local and/or nonlinear bulk deformation region near the cohesive zone, the results of the FPM with a finite number *N* must be interpreted as J-equivalent cohesive zone behaviour. In other words, the FPM is regarded as a mechanical test in which the region enclosed by the elastic field is energetically stimulated by the J-interaction integral operations with appropriate eigenfunction fields, and the $\mathbf{g}_n$, $\mathbf{h}_n$, $\mathbf{q}_n$, and $\mathbf{r}_n$ values determined by the interaction J integrals are considered as responses to such mechanical stimuli. The responses of the J-evaluated $\mathbf{g}_n$ are interpreted as cohesive zone tractions of a J-equivalent cohesive zone, while those of the J-evaluated $\mathbf{h}_n$ are understood as cohesive zone separation gradients of the J-equivalent cohesive zone. Similarly, the responses of the J-evaluated $\mathbf{q}_n$ are taken as the surface stress gradient of the J-equivalent cohesive zone, and the responses of the J-evaluated $\mathbf{r}_n$ are taken as the CCL displacement gradient of the J-equivalent cohesive zone.

In the following section, the FPM is utilised to probe the J-equivalent cohesive zone characteristics of atomic decohesion in a $[\bar{1}\bar{1}2]$ direction on a (111) plane of a gold single crystal, with crack tip deformation fields from EAM simulations. In the analysis, it is found that N=3 with an optimum cohesive zone size is enough to describe the J-equivalent cohesive zone characteristics, since the self-equilibrium fields of the high spatial frequency traction distribution at the cohesive zone rapidly decay away from the cohesive zone. Even though the field projection scheme described so far is formulated for general anisotropic bi-materials, degenerate cases in which one or both of the constituent materials are isotropic can be dealt with in the same framework, as discussed by Choi et al. [37], for a sharp crack tip field. Also, it is worth mentioning that for special combinations of anisotropic bi-materials, e.g. symmetric tilt grains, of which the bi-material matrix, $\mathbf{M}_{<1>}^{-1}+\bar{\mathbf{M}}_{<2>}^{-1}$, is a real symmetric matrix, the oscillatory stress fields disappear and many of the mathematical expressions involved in the field projection can be reduced to very simple forms with the relations $\boldsymbol{\beta}=\mathbf{0}$ ($\varepsilon=0$), $\mathbf{Y}[\eta(z)]=\mathbf{I}$, $\mathbf{V}\bar{\mathbf{V}}^T=\mathbf{L}_{<1>}^{-1}+\mathbf{L}_{<2>}^{-1}$, and $\tilde{\mathbf{P}}_n(z)=\mathbf{I}U_n(z)$.

6. EAM Simulation and Field Projection of Atomic Decohesion in Gold

6.1 Atomistic deformation analysis with EAM simulations

In a cohesive zone framework, the constitutive relations of the cohesive zone are regarded as phenomenological material characteristics that can be evaluated by the FPM described in the previous section. The FPM is applicable to the decohesion processes in homogeneous elastic solids, as well as to those of interfaces in anisotropic elastic bi-materials. The application of the method is also valid for any elastic deformation fields of cohesive crack-tips obtained either by experimental measurements or by computational simulations. In this section, the FPM is applied to analysing nano-scale decohesion processes and their associated deformation fields in a face-centeredcentred cubic gold crystal, obtained by atomistic simulations. The EAM potential of Foiles et al. [9] is employed for the atomistic simulations since the potential is known to be quite reliable for atomistic simulations of atoms with nearly-filled d-orbital electronic configurations such as gold. Foiles et al. [9] provided the potential tuned to fit various empirical material parameters including the lattice constant of gold, $a = 4.08$ Å, the three elastic constants of $C_{11} = 183.0 \text{ GPa}$, $C_{12} = 159.0 \text{ GPa}$, and $C_{44} = 45.0 \text{ GPa}$, the sublimation energy of 3.93 eV, and the vacancy formation energy of 1.03 eV. They also reported that the potential gives a (111) surface energy of 0.79 Jm^{-2} and a surface relaxation of 0.1 Å contraction in the first layer of a (111) free surface.

In this study, the crack geometry of a (111) plane decohesion is considered. A semi-infinite crack is on a (111) plane with its crack tip lying along a $[\bar{1}10]$ direction and its prospective propagation direction in $[\bar{1}\bar{1}2]$. A Cartesian coordinate system is assigned with the x_1' axis along $[\bar{1}\bar{1}2]$, the x_2' axis along $[111]$, and the x_3' axis along $[\bar{1}10]$ for the deformation analysis.

In the atomistic field of an embedded atom method potential, the deformation is nonlocal and it can be induced by nearby density gradients; for example, the surface relaxation is evident near a free surface in the atomistics. Therefore, a local deformation associated with a stress field must be delineated from such atomistic nonlocal deformations near a free surface[9]. Here, “local” constitutive relation signifies that the stress is only a function of the stress-inducing strain at a local point. However, it is quite difficult to find the stress-inducing deformation from the final equilibrium positions of the atoms for a crack tip geometry, because the stress-free reference configuration is not well defined near the crack tip for the nonlocal atomistics. In the following, a construction of an approximate stress-free reference configuration is introduced. The approximate reference configuration is close to a stress-free state away from the crack tip. Since the field projection method utilizes the far-field information, it is sufficient to use the approximate reference configuration, in extracting the crack tip cohesive zone constitutive relations with the field projection method. Derivation of the stress-inducing deformation from the approximate stress-free reference configuration involves four atomistic configurations.

Figure 3 shows the four configurations of the atomistic states. The black and white atoms in figure 3 represent atoms in different $(\bar{1}10)$ atomic planes, e.g. the A and B atomic planes, respectively, which are considered to be the planes of the generalised two-dimensional deformation. The top half of figure 3(a) shows a perfect lattice configuration and the bottom bright region depicts a continuum representation of the perfect lattice. Figure 3(b) exhibits an atomistic equilibrium state of a deformed configuration. The top half of figure 3(c) demonstrates an atomistic configuration relaxed near a free surface along the x_1' axis and the bottom dark region illustrates a continuum representation of the relaxed configuration. Figure 3(d) shows a hybrid configuration of the perfect lattice configuration (a) and the relaxed free- surface configuration (c).

The deformed configuration in equilibrium, shown in figure 3(b), was generated by relaxing the atomic positions from an imposed initial configuration, while the atomic positions at an outer boundary layer were held fixed. The initial configuration corresponds to a linear elastic crack-tip displacement field of a mixed mode with $K_I = 0.38\ \mathrm{MPa}\sqrt{\mathrm{m}}$ and $K_{II} = -0.10\ \mathrm{MPa}\sqrt{\mathrm{m}}$. The initial condition was imposed on 98,496 gold atoms in the region of three dimensions: $54\sqrt{6}a \times 76\sqrt{3}a \times \sqrt{2}a$. Then, a conjugate gradient method of minimising the total energy of the system was used to relax the atomic positions in the bulk region, while the atoms at the outer boundary layer, with a thickness of $2a$, were held fixed and periodic boundary conditions were applied in a $[\bar{1}10]$ direction. The total energy of the system at each stage of the relaxation was evaluated using the EAM potential of Foiles et al. [9]. The mode mixity of the initial condition was chosen to suppress the localised deformation along the $[112]$ direction on a $(11\bar{1})$ plane, which could have emitted a dislocation during the relaxation if the mode mixity had not been applied. In the following section, the decohesion process zone ahead of the crack tip in figure 3(b) is analysed with the FPM developed in the previous sections.

In the following deformation analysis, the atomic positions on only one atomic plane, e.g. plane A in figure 3, are used for the planar field projection analysis. Here, the j'th atomic position in a perfect lattice (figure 3(a)) is denoted as $\boldsymbol{x}'^{j}_{[\mathrm{P}]}$, in the cracked configuration (figure 3(b)) as $\boldsymbol{x}'^{j}_{[\mathrm{C}]}$, in a free surface relaxed configuration (figure 3(c)) as $\boldsymbol{x}'^{j}_{[\mathrm{F}]}$, and in a hybrid reference configuration (figure 3(d)) as $\boldsymbol{x}'^{j}_{[\mathrm{R}]}$. The hybrid reference position is defined as

$$\boldsymbol{x}'^{j}_{[\mathrm{R}]} \equiv \frac{|\theta|}{\pi}\boldsymbol{x}'^{j}_{[\mathrm{F}]} + \left(1 - \frac{|\theta|}{\pi}\right)\boldsymbol{x}'^{j}_{[\mathrm{P}]}, \tag{16}$$

where the angle θ is measured from the prospective crack propagation direction to the line segment between $\boldsymbol{x}'^{j}_{[\mathrm{P}]}$ and the crack tip. We also define the deformation gradient from $d\boldsymbol{x}'_{[\mathrm{P}]}$ to $d\boldsymbol{x}'_{[\mathrm{C}]}$ as $\boldsymbol{F}_{[\mathrm{C}]}$, from $d\boldsymbol{x}'_{[\mathrm{P}]}$ to $d\boldsymbol{x}'_{[\mathrm{R}]}$ as $\boldsymbol{F}_{[\mathrm{R}]}$, and from $d\boldsymbol{x}'_{[\mathrm{R}]}$ to $d\boldsymbol{x}'_{[\mathrm{C}]}$ as $\boldsymbol{F}_{[\mathrm{H}]}$. Every deformation gradient of a configuration relative to a perfect lattice configuration, such as $\boldsymbol{F}_{[\mathrm{C}]}$ or $\boldsymbol{F}_{[\mathrm{R}]}$, can be defined in the Voronoi cell [38] of the j 'th atom in the perfect lattice configuration as

$$\boldsymbol{F}^{j} \equiv \frac{1}{A_0}\sum_{k=1}^{N}\left[\left(\frac{\boldsymbol{x}'^{j(k)} - \boldsymbol{x}'^{j}}{2}\right)\otimes \boldsymbol{n}^{k}\right]\Delta L_0^{k}\ , \tag{17}$$

where $\boldsymbol{n}^{k}$ and ΔL_0^{k} are the outward unit normal vector and the length of the k 'th side of the Voronoi cell, respectively; $\boldsymbol{x}'^{j(k)}$ is the position of the nearest atom in the $\boldsymbol{n}^{k}$ direction; and A_0 is the area of the Voronoi cell. Equation (17) is for a two-dimensional case with $N = 4$. Then, the deformation gradient $\boldsymbol{F}^{j}_{[\mathrm{H}]}$ of the cracked configuration (b) with respect to the hybrid reference configuration (d) is given by $\boldsymbol{F}_{[\mathrm{H}]} = \boldsymbol{F}_{[\mathrm{C}]}\boldsymbol{F}^{-1}_{[\mathrm{R}]}$. Defining the deformation gradient at a surface atomic site, the relative displacement at the free-surface-side face of the Voronoi cell, with respect to the displacement at the atomic site, is chosen to be equal to the negative of the displacement at the opposite face of the Voronoi cell. When the hybrid reference configuration is used to evaluate the deformation gradient, the deformation gradient near the free surface is scarcely sensitive to the choice of the relative displacement.

When an atomistic deformation field is analysed with a local elasticity theory, we must consider two major effects of the high atomic density gradients near a free surface. One is the surface stress effect and the other is the surface relaxation effect. The surface stress effect is taken into consideration in the configurational force balance, as shown in figure 2. The surface relaxation effect is dealt with by the proper choice of an effective reference configuration for assessing the deformation that induces bulk stress. The hybrid reference configuration, $\boldsymbol{x}'^{j}_{[\mathrm{R}]}$ of figure 3(d), is used in this paper as the effective reference configuration. Since the FPM uses an elastic field at a distance away from the crack tip, the hybrid reference configuration is a satisfactory choice. Figure 4(a) shows a vector plot of the displacement gradient in the x'_2 direction, $(F_{12[\mathrm{P}]},\ F_{22[\mathrm{P}]} - 1)$, with respect to the perfect lattice reference configuration. The plot exhibits a very large displacement gradient of the surface relaxation, which cannot be used for evaluating the bulk stress induced by elastic deformation. Figure 4(b) shows $(F_{12[\mathrm{H}]},\ F_{22[\mathrm{H}]} - 1)$ with respect to the hybrid reference configuration. The figure shows the elimination of the artefact of the displacement gradients caused by the surface relaxation. Therefore, the hybrid deformation gradient was used for the linear strain tensor, $\boldsymbol{\varepsilon} = (\boldsymbol{F}_{[\mathrm{H}]} + \boldsymbol{F}_{[\mathrm{H}]}^T)/2 - \boldsymbol{I}$, to evaluate the bulk stress, $\boldsymbol{\sigma} = \boldsymbol{C} : \boldsymbol{\varepsilon}$, at a region of small strain, where the interaction J integrals of the FPM were carried out. For the integration, the deformation gradient was linearly interpolated between the atomic positions. For numerical accuracy the interaction integrals, $J_{\Gamma_o}^{\mathrm{int}}[S, \hat{S}]$ in equation (5) were evaluated with domain integrals [39]. The width of the integration domain, D in figure 2, was set to be 20 Å, while the rectangular inner boundary of the domain surrounded the cohesive zone at a distance d, having a dimension of $2d$ by $2(c+d)$ with d=10 Å.

6.2 Field projection of the atomistic deformation field

The interaction domain integrals $J_D^{\mathrm{int}}[S, \hat{S}]$ between the atomistic deformation field $S[\boldsymbol{\sigma}, \boldsymbol{u}]$, e.g. figure 3(b), obtained from the EAM analysis and the auxiliary eigenfunction fields $\hat{S}[\boldsymbol{\sigma}, \boldsymbol{u}]$ developed in section 5 are calculated for the FPM to evaluate the cohesive zone characteristics. The cohesive zone characteristics are described by $\mathbf{g}_n$, $\mathbf{h}_n$, $\mathbf{q}_n$, and $\mathbf{r}_n$ $(n = 0, 1, 2, \cdots, N)$ of the equations (15a-d) and the cohesive zone end locations. In the following analysis, n up to 2 is used so that the cohesive zone characteristics are effectively described with 38 parameters: three components of the twelve coefficient vectors and the two end positions of the cohesive zone. The two end positions of the cohesive zone were chosen as $x_1^a = -14$ Å and $x_1^b = 109$ Å ($c = 61.5$ Å) by trial and error so that at the left end position, x_1^a, and the cohesive zone normal separation, δ_2, obtained from the FPM is as close as possible to that of the applied linear elastic K-field, and at the right end position, x_1^b, the cohesive zone normal traction, t_2, has the same value as that of the applied K-stress field. The location of the left end position, $x_1^a = -14$ Å, estimated by the FPM is approximately one lattice distance, 4 Å, from the location, $x_1' \cong -10.0$ Å, where the distance between the nearest atoms in the upper and lower surfaces is approximately equal to the cut off radius of inter-atomic interaction in gold, 5.55 Å. The difference is believed to be caused by the surface stress employed in the cohesive zone model and by the choice of the criterion to match the normal separation, δ_2, obtained from the FPM to that of the applied linear elastic K-field.

Figures 5(a) and (b) respectively show the cohesive zone tractions and separations determined by the FPM for the atomistic deformation field simulated with the displacement boundary conditions of the applied linear elastic K-field. The cohesive zone shear traction, t_1, shown in figure 5(a) deviates from that of the applied linear elastic K-field near the right end of the cohesive zone. In this crystallographic orientation of a face-centred cubic crystal, the opening and shearing modes are coupled together from the linear elastic point of view. In other words, the tangential separation is related not only to the shear traction, but also to the normal traction and similarly for the normal separation; thus, the opening and the shearing modes should be considered together. The mixed mode dependence is approximately 3 % of the primary mode dependence in this orientation. If the mixed mode dependence is ignored, the two modes can be separated and the cohesive zone shear traction, t_1, at the right end position, x_1^b, can be matched to that of the applied K -stress field by adjusting $x_1^b = 160$ Å ($c = 87.0$ Å), as shown with the dash-dot curve in figure 5(a). However, since the cohesive zone shear tractions for the two different cohesive zone sizes give similar results for the surface stress and surface energy distributions in the cohesive zone, the two end positions of the shear cohesive zone are set to be the same as those of the normal cohesive zone. The shear separations shown in figure 5(b) for the two different cohesive zone sizes are very close to each other. The normal separation, shown as a dark solid curve in the figure, exhibits a zone of negative separation between $x_1' \cong 18$ Å and $x_1' \cong 62$ Å. This is a sub-region of the negative normal separation modulus in the cohesive zone, which may reflect the tendency of phase transformation such as twinning or unstable shear localisation in a certain slip plane near the crack tip.

Figures 6(a) and (b) show the surface stress gradients and centre line displacements of the cohesive zone, respectively. A careful observation of the equilibrium atomic positions near the crack tip reveals that the inter-atomic crack plane is not flat: it is curved. Therefore, the surface stress and the curvature can sustain the normal traction jump, i.e. the normal surface stress gradient. T -stress is believed to cause significant variations of the curvature to change the normal surface stress gradient. The relationships between the cohesive zone tractions and separations are plotted in figure 6(c). The maximum normal traction in the cohesive zone is 4.06 GPa when $\delta_2 = 0.29$ Å. The cohesive zone surface stress is plotted against the normal separation along the cohesive zone in figure 6(d). The surface stress is a monotonically increasing function of the normal separations, δ_2, except for the small δ_2. The surface stress of the (111) free surface in the [112] orientation is $2.06\ \mathrm{Nm}^{-1}$

7. Discussions

Before the results of the field projection for atomistic decohesion in gold are discussed, three major approximations employed in this analysis are explained briefly. One is for deformation non-locality, another for deformation nonlinearity, and the other for the numerical integration employed in the FPM. Firstly, the deformation field analysed by the EAM is inherently non-local. The non-locality is projected onto a planar region while the material behaviour at the atomistic scale in the remainder of the bulk region is treated with a local theory of linear elasticity. Secondly, there is some nonlinear deformation outside the cohesive zone. The nonlinearity is also projected onto the cohesive zone in this field projection scheme. Finally, since the deformation gradients are linearly interpolated between atomic positions, the lattice constant of gold, $a = 4.08$ Å, acts as a fundamental length scale and the integration becomes inaccurate along a contour close to the cohesive zone for a small c/a. As Hong and Kim [11] noted, the interaction integral turns out to be subtracting a large number from another large number to obtain a small value of the integral for a large c/a and a large number of series terms, n. Therefore, the integration is performed at an optimum distance from the cohesive zone with a finite n. The truncation of the series of eigenfunctions for the field projection implies a low spatial frequency representation of the distribution of the cohesive zone characteristics. It is also worth noting that the linear strain tensor is used in the interaction integral to guarantee path independence, and thus, the domain of the integral avoids a region of large rotation.

The results of the field projection presented in the previous section show various cohesive zone characteristics that can be interpreted in a continuum point of view for atomistic decohesion in a discrete lattice system of a gold crystal. Comparisons between the characteristics in the view of a continuum and those derived somewhat directly from the atomic positions are discussed here. In figure 7(a), the field projected normal and shear separations shown in figure 5(a) are compared with the atomic site separations between adjacent atomic planes across the cohesive zone. The atomic site separations stand for the difference between the displacement at an atomic site on one of the two separating atomic planes and the displacement at the conjugate counter point on the opposite atomic plane of separation. The conjugate counter point is a Lagrangian point where a vector normal to the separating atomic plane at an atomic site intersects with the opposite separating atomic plane in the reference configuration. The atomic site normal separations, shown as solid circles in figure 7(a), display a sharp transition at the crack tip, while the atomic site shear separations, shown as open circles, demonstrate a smooth transition. The distribution of the atomic site shear separations is far more spread in the cohesive zone than that of the normal separations because the inter-atomic plane of decohesion is an easy-glide slip plane. On the other hand, the field projected normal separation oscillates smoothly along the atomic site separation distribution. The field projected shear separation closely follows the distribution of the atomic site shear separation. The field projected separation distributions resemble low frequency approximations of the atomic site separations in the cohesive zone. It is also worth noting that the atomic site separations are evaluated with the displacements on two separating atomic planes, while the continuum separations are determined by the displacements extrapolated to the mid-plane of the two separating atomic planes.

Once the separations in a cohesive zone are known, the tractions in the cohesive zone have traditionally been estimated with rigid separation potentials, e.g. Rose et al. [40], or with generalised stacking fault energy, e.g. Vitek [41]. For a combined normal and shear separation of two atomic planes, two simple processes of separation can be considered. One is the rigid separation for which the relative atomic positions are held rigid, respectively, in each volume of the two separating parts; the other is the affine separation for which all atomic inter-planes parallel to the decohesion plane of interest experience the same separations. If the inter-atomic potential were local, the energy per unit area required for a rigid separation, i.e. the rigid separation potential, would be identical to that for a corresponding affine separation. In figure 7(b), the rigid separation potential corresponding to every atomic site separation in the cohesive zone is plotted with a dark solid circle, while the affine potential at every matching site is mapped out with an open circle. The two separation processes are substantially different with respect to each other indicating that the inter-atomic potential is non-local, particularly for large deformations. The non-locality in the EAM potential occurs for two major reasons. One is that an atom interacts with atoms beyond the nearest neighbours, with a cut off radius of 5.55 Å in gold, and the inter-atomic potential is anharmonic; the other is that the embedding term in the EAM potential is a nonlinear function of electron density and the background electron density is a superposition of the atomic electron densities of atoms hosting the embedding. The latter reason is solely responsible for the difference between the complete separation energy of the rigid and affine separations, while both reasons are accountable for the non-local elastic behaviour of the solid when the strain gradient is large. This fact signifies that the fracture energy of nano-scale decohesion depends on the history of the deformations adjacent to the decohesion process zone, even without a dislocation motion. In fracture mechanics terms, the critical stress intensity factors for a nano-scale decohesion process depend on various non-singular stress terms, including the T -stress; the fracture toughness depends on external loading. In addition, the non-local effects, together with the discreteness of the lattice, determine the lattice trapping toughness variation of the crack tip at the nano-scale.

Figure 7(b) also shows the field-projected decohesion potential $\Pi\left(x'\right)$, with a dark solid curve, as a function of the position x_1' along the cohesive zone:

$$\Pi\left(x_1'\right)=\int_c^{x_1'}\left(t_2^a\frac{d\delta_2}{dx_1}+t_1^a\frac{d\delta_1}{dx_1}\right)dx_1+\int_c^{x_1'}\left(\tau_2\frac{du_2^a}{dx_1}+\tau_1\frac{du_1^a}{dx_1}\right)dx_1\ . \tag{18}$$

The decohesion potential is composed of the separation potentials expressed as the first integral in equation (18) and also contributions from the surface stress articulated in the second integral. The separation potential can be decomposed into a normal separation potential (the thin dashed line in figure 7(b)) and a shear separation potential (the thin dash-dot curve in figure 7(b)). The contribution from the surface stress is so small that it cannot be seen in the plot of figure 7(b). The complete decohesion potential at the left end of the cohesive zone is 1.407 Jm^{-2}, which is approximately 2 % smaller than the J integral value around the cohesive zone. This difference is believed to be a truncation error of the eigenfunction series in the FPM. The potential shows that the major decohesion process occurs in the range of -14 Å $< x_1' <$ 18 Å, and a region of negative potential appears at approximately 18 Å $< x_1' <$ 65 Å. Twice the surface stress, 2Σ, distributed in the cohesive zone is plotted in the thick dashed line in figure 7(b). The surface stress mostly develops in the range of -14 Å $< x_1' <$ 50 Å. These region sizes represent the effects of the atomistic deformation non-locality reflected on the cohesive zone model through a low-spatial-frequency field projection. The fully developed surface stress in the $[\bar{1}\bar{1}2]$ direction on the (111) face is estimated to be 1.05 Nm^{-1} in this analysis.

Regarding the distribution of potentials in the cohesive zone, the sizes of the cohesive zone and the sub-zone of the negative potential are surprisingly large. Although the cut off spatial frequency involved in the field projection was low for the given cohesive zone size, the cohesive zone size was an optimisation parameter for the field projections shown in figure 7(b). Therefore, the large optimum size of the cohesive zone, 12.3 nm, and the existence of a relatively large sub-zone of negative potential appear to indicate the tendency for unstable phase transformations, such as twining or dislocation emission, near the crack tip. Indeed, localised twinning was observed ahead of the crack tip when the magnitude of the applied K_{II} was increased, keeping the sign of the mode mixity. When the sign of the mode mixity was reversed, a dislocation was emitted on a $(11\bar{1})$ plane in a $[112]$ direction, as shown in figure 3(b). The tendency of the non-local elastic field to drive such unstable deformations near the crack tip is believed to be projected on the cohesive zone as a zone of negative decohesion potential or negative modulus.

The energy release rate of the crack was also evaluated by the J integral and interaction J integrals, based on various deformation gradients that were defined differently for the atomistic deformation field. The inner contours of the domain integral were squares made of $|x_1'| = c'$ and $|x_2'| = c'$ with a constant c' ranging from 5 to 200 Å. The results are shown in figure 8. Regarding the field without an applied T-stress shown in figure 8(a), the energy release rates, as evaluated by the J integral with the hybrid deformation gradient $\boldsymbol{F}_{[\mathrm{H}]}$, are shown with open circles and they are path independent for a c' larger than approximately 60 Å. Even in the range 5 Å $\le c' \le$ 60 Å, the J integral values are nearly path independent. The J values are approximately 1.5 – 2 % lower than the applied nominal J value, 1.475 Jm^{-2}, of the displacement field at the outer boundary layer of the modelling region. The differences are believed to be mainly due to the relaxation from the initial field to an equilibrium field within a finite modelling volume. The results of the evaluation of the J integrals with the deformation gradient, $\boldsymbol{F}_{[\mathrm{C}]}$, relative to a perfect lattice configuration are plotted with solid circles and underestimate the energy release rate by approximately 10 %. The energy release rate was also evaluated by interaction J integrals with both the hybrid deformation gradient, $\boldsymbol{F}_{[\mathrm{H}]}$, and the deformation gradient, $\boldsymbol{F}_{[\mathrm{C}]}$, relative to a perfect lattice configuration; the former is plotted with open squares and the latter with solid squares. For the auxiliary field of the interaction J integrals, the singular K -field of a crack tip in an anisotropic elastic solid with the same orientation was employed. Then, the complex stress intensity factor K was converted to the energy release rate. The energy release rates evaluated by the interaction J integrals were almost identical to the J values computed with the hybrid deformation gradient. The interaction J integral evaluations were insensitive to the choice of reference configurations between the perfect and hybrid configurations. The energy release rates estimated with the low spatial frequency field projection are also outlined in figure 8. The energy release rate assessed by the complete decohesion energy is the same as that assessed by the complete separation energy; the contributions from the surface stress are negligible for this field. In order to see the path dependence of the field projection, one-eighth of the perimeter size of the rectangular contour was used as the average contour size in this plot. The energy release rates estimated by the field projection were independent of the contour size.

As shown in figure 8, the low spatial frequency field projection with an n up to 2 in equation (15) imparts an approximately 2 % truncation error in the energy release rate estimation. If the Griffith criterion [42] were satisfied for an equilibrium crack-tip field in the nano-scale, the energy release rates evaluated by the J integral would be identical to $2\gamma_0$ for a field without T -stress and $2\gamma_0 + 2\Sigma_0\varepsilon_T$ for a field with T -stress. On the contrary, the near-crack-tip non-local deformation field allows variation of the atomistic configuration to induce an apparent lattice trapping barrier for crack growth. Considering that the critical energy release rate, $\mathcal{G}$, for a crack growth rate, $\dot{l}$, should satisfy the dissipation condition, $(\mathcal{G} - 2\gamma)\dot{l} \geq 0$, there is an admissible range of surface energy at $\mathcal{G}_{\mathrm{rec}} \leq 2\gamma \leq \mathcal{G}_{\mathrm{adv}}$, where $\mathcal{G}_{\mathrm{rec}}$ and $\mathcal{G}_{\mathrm{adv}}$ denote the critical energy release rates for crack recession (or healing) and advancement, respectively.

In order to see the lattice trapping effect, the applied mode I stress intensity factor was varied in the range of $0.375\ \mathrm{MPa}\sqrt{\mathrm{m}} \leq K_I \leq 0.385\ \mathrm{MPa}\sqrt{\mathrm{m}}$, while the mode II stress intensity factor was maintained at $K_{II} = -0.10\ \mathrm{MPa}\sqrt{\mathrm{m}}$. Neither crack propagation nor healing was observed in the range of $0.376\ \mathrm{MPa}\sqrt{\mathrm{m}} \leq K_I \leq 0.384\ \mathrm{MPa}\sqrt{\mathrm{m}}$. However, when $K_I = 0.375\ \mathrm{MPa}\sqrt{\mathrm{m}}$ or $K_I = 0.385\ \mathrm{MPa}\sqrt{\mathrm{m}}$ was applied, a dislocation was emitted from the crack tip on the $(11\bar{1})$ plane along the [112] direction. It is an interesting result that a crack does not advance or heal. Therefore, it can be known that $\mathcal{G}_{\mathrm{rec}} \leq 1.38\ \mathrm{Jm}^{-2}$ and

1.44 Jm^{-2} $\le G_{\mathrm{adv}}$. Considering that the $2\gamma_0$ of the (111) free surface is approximately 1.58 Jm^{-2} for the EAM potential [9], the lattice trapping magnitude of the energy release rate for crack healing is more than 14 % of $2\gamma_0$. Although a full study of the critical conditions of lattice trapping and dislocation emission is beyond the scope of this paper, it has been demonstrated that a proper choice of hybrid reference configuration makes it possible to evaluate the J integral values accurately and thus, to study such critical crack tip conditions. While conventional J integral evaluations with a proper hybrid configuration can provide accurate energy release rates, the FPM offers a means of studying the cohesive zone characteristics, in particular the sizes of the non-local and nonlinear deformation zones and definitions of tractions, at the atomistic length scale in the cohesive zone.

Figure 9 shows the states of the nominal normal separations and tractions in the cohesive zone measured by the rigid separation potential (RSP) method and by the FPM. In figure 9(a), the solid circles indicate the states determined by the RSP method at the atomic sites in the cohesive zone. The states of the RSP of the normal separations with various constant shear separations are also illustrated with various curves. The nominal normal peak stress is approximately 14 – 15 GPa; although it can be reduced by a certain amount with a superimposed shear separation, it is larger than 10 GPa for shear separations less than 80 % of the unstable stacking shear separation. However, the field projected states of the normal separations are quite different from those of the RSP and are plotted with a thick line in the figure. The FPM gives a normal peak stress of only 4 GPa. Figure 9(b) exhibits the atomic positions near the decohesion process zone. The fifth atom is at the RSP state of 12 GPa nominal normal peak stress; however, the FPM measures the peak stress of 4 GPa at the tenth atom in the numbering sequence. The RSP measurements indicate that the inter-atomic forces are transmitted through the atomic bonds of the second atom and beyond; however, the FPM shows that the forces are transmitted through those of the first atom and beyond. In the RSP measurements, only one isolated atom, number 5, experiences a nominal normal stress above 4 GPa; the nominal traction at such an isolated site cannot be assessed reliably by the RSP. The FPM provides an estimation of the traction from extrapolations of the adjacent inter-atomic states. The field projection shows that the cohesive zone tractions are more broadly spread than the distribution measured by the RSP method.

8. Conclusions

A general formulation of a planar elastic field projection has been derived for identifying the cohesive zone constitutive relations from the static or steady state dynamic elastic fields of a cohesive crack tip on an interface between two anisotropic solids. The formulation is also applicable to the elastic field of a cohesive crack tip in a homogeneous solid whether it is isotropic or anisotropic. A new framework of cohesive zone models, including the surface stress effects, has been introduced to develop the nano-scale FPM. A new eigenfunction expansion of the elastic field surrounding a crack-tip cohesive zone made it possible to develop the FPM. The eigenfunctions were orthoginalised for interaction J integrals based on the Jacobi polynomials. The field projection using the interaction J integrals provides J-equivalent cohesive tractions, interface displacements and separations, as well as the surface energy gradients caused by the gradual variation of the surface formation within the cohesive zone. In particular, the FPM can define tractions and stresses within and near a cohesive zone more objectively than the conventional rigid separation potential method. In addition, the field projection measurement can identify the energetic states of decohesion in the cohesive zone and it provides a means to compare the experimental measurements and computational simulations of atomistic decohesion or slip processes on the same grounds.

The efficacy of the FPM has been demonstrated with nano-scale deformation fields of EAM atomistic simulations for crystal decohesion along a $[\bar{1}\bar{1}2]$ direction in a gold (111) plane. It has been noticed that two major free surface effects, i.e. surface relaxation and surface stress, play significant roles in the atomistic elastic field analysis near a crack tip. The surface stress has been correctly incorporated into the relationship of the configurational force balance in the cohesive zone model and a hybrid reference configuration has been introduced to deal with the surface relaxation effect. These two new treatments have made it possible to study lattice trapping in crack growth and the validity of the Griffith criterion with conservation integrals. It has been found that the lattice trapping potential is larger than 14 % of $2\gamma_0$ for the healing process of a gold (111) plane in a [112] direction. The low spatial frequency field projections have revealed that the decohesion potential along the cohesive zone is quite different from the prediction based on the rigid separation potential. The peak normal traction, approximately 4 GPa, in the cohesive zone has been found to be much lower than the 15 GPa expected from the rigid separation potential. This result clearly shows that the rigid separation potential overestimates the peak stress of separation in the crack tip region of highly nonlocal deformation. It has been also noticed that the critical energy release rates for various crack tip processes, such as crack growth and dislocation emission, depend heavily on the modes, such as $K_{\mathrm{II}} / K_{\mathrm{I}}$ and the T -stress, of external loading on the crack tip at the nano-scale. The field projection also showed that a sub-zone of negative potential exists within the cohesive zone, reflecting the tendency of some unstable deformations near the crack tip and that the effective cohesive zone size varies depending on the mode of external loading. Half of the effective zone size, which is presumably close to the radius of the non-local deformation zone, was measured to be approximately $40\,\text{Å}$ in an applied singular field. The FPM, together with the various analysis techniques developed in this paper, will be useful in studying decohesion, dislocation emission, single asperity friction, and grain boundary sliding and separations in crystalline solids in the nano-scale.

Acknowledgements

This work was supported by the MRSEC Program of the National Science Foundation under Award Number DMR-0079964 and the Post-Doctoral Fellowship Program of Korea Science & Engineering Foundation (KOSEF). The authors are grateful to Dr. Pranav Shrotriya for his help with the code Dynano87 for the atomistic simulations and Dr. Foiles for making the code available to the public on ftp://146.246.250.1.

Appendix A: Stroh matrices $\mathbf{A}$, $\mathbf{B}$, and $\mathbf{M}^{-1}$

Among the expressions of the displacement and stress fields of an anisotropic elastic medium presented in equations (1) and (2) of the main text, the terms entering the expressions of the boundary conditions along the entire x_1 axis are

$$\{\boldsymbol{e}_1 \cdot \nabla \boldsymbol{u}\} = 2\,\mathrm{Re}\left[\mathbf{A}\mathbf{f}'(z)\right], \tag{A1a}$$

$$\{\boldsymbol{e}_2 \cdot \boldsymbol{\sigma}\} = 2\,\mathrm{Re}\left[\mathbf{B}\mathbf{f}'(z)\right], \tag{A1b}$$

where $\boldsymbol{e}_1$ and $\boldsymbol{e}_2$ represent the base vector of the (x_1, x_2) Cartesian coordinate. The symbol $\mathbf{A}$ represents a complex matrix that satisfies the Stroh [28] characteristic equations

$$\left[\{\boldsymbol{T}_a\} + \{\boldsymbol{T}_b + \boldsymbol{T}_b^T\}\tilde{\lambda} + \{\boldsymbol{T}_c\}\tilde{\lambda}^2\right]\mathbf{A}^T = \mathbf{0} \tag{A2}$$

with $\boldsymbol{T}_a = \boldsymbol{e}_1 \cdot \boldsymbol{C} \cdot \boldsymbol{e}_1$, $\boldsymbol{T}_b = \boldsymbol{e}_1 \cdot \boldsymbol{C} \cdot \boldsymbol{e}_2$, $\boldsymbol{T}_c = \boldsymbol{e}_2 \cdot \boldsymbol{C} \cdot \boldsymbol{e}_2$, $\boldsymbol{C}$ denotes the elastic moduli tensor of the solid, and $\tilde{\lambda}$ is the diagonal Stroh eigenvalue matrix with the components of $p_j \delta_{jk}$. The matrix $\mathbf{B}$ is given by

$$\mathbf{B} = \{\boldsymbol{T}_b^T\}\mathbf{A} + \{\boldsymbol{T}_c\}\mathbf{A}\tilde{\lambda}. \tag{A3}$$

Stroh [28] showed that $\mathbf{A}$ and $\mathbf{B}$ are non-singular for three distinct complex pairs of p_j and the matrix

$$\mathbf{M}^{-1} \equiv i\mathbf{A}\mathbf{B}^{-1} \tag{A4}$$

is a positive definite Hermitian matrix. Here, $i = \sqrt{-1}$ and $()^{-1}$ stands for the inverse of the matrix. The explicit expressions of $\mathbf{A}$, $\mathbf{B}$, and $\mathbf{M}^{-1}$ in terms of elastic constants are given in Suo [30] [Suo used the symbols $\mathbf{L}$ and $\mathbf{B}$ in his paper for $\mathbf{B}$ and $\mathbf{M}^{-1}$ in this paper, respectively.] and Ting [43].

Appendix B: A complex function representation of the anisotropic elastic field of a bi-material interface crack tip

The eigenfunction expansion around a sharp interfacial crack tip lying on the negative x_1 axis in an anisotropic bi-material is given by Beom and Atluri [32] as

$$\mathbf{f}'_{<\mu>}(z) = \mathbf{B}^{-1}_{<\mu>} \left\{ \left[\mathbf{I} - (-1)^{\mu} i \boldsymbol{\beta} \right] \mathbf{Y}\left[z^{-i\varepsilon} \right] \frac{\mathbf{k}(z)}{2\sqrt{2\pi z}} + i \left[\mathbf{I} - (-1)^{\mu} \boldsymbol{\alpha} \right] \mathbf{m}(z) \right\}, \tag{B1}$$

for $\mu = 1 \text{ or } 2$ referring to materials 1 or 2, respectively, and where $\mathbf{k}(z)$ and $\mathbf{m}(z)$ are real analytic functions that satisfy $\mathbf{k}(z) = \bar{\mathbf{k}}(z)$ and $\mathbf{m}(z) = \bar{\mathbf{m}}(z)$, respectively. The generalised Dundurs parameter matrices $\boldsymbol{\alpha}$ and $\boldsymbol{\beta}$ for dissimilar anisotropic materials are defined as follows [32, 33]:

$$\boldsymbol{\alpha} = \left(\mathbf{L}_{<1>} - \mathbf{L}_{<2>} \right) \left(\mathbf{L}_{<1>} + \mathbf{L}_{<2>} \right)^{-1}, \quad \boldsymbol{\beta} = \left(\mathbf{L}^{-1}_{<1>} + \mathbf{L}^{-1}_{<2>} \right)^{-1} \left(\mathbf{W}_{<1>} - \mathbf{W}_{<2>} \right), \tag{B2}$$

where $\mathbf{L}^{-1} = \mathrm{Re}\left(\mathbf{M}^{-1} \right)$ is a symmetric real matrix and $\mathbf{W} = -\mathrm{Im}\left(\mathbf{M}^{-1} \right)$ an anti-symmetric real matrix and, thus, $\boldsymbol{\alpha}$ and $\boldsymbol{\beta}$ are also real matrices. The bi-material parameter ε that appears in the argument of the function $\mathbf{Y}[z^{-i\varepsilon}]$ is an oscillatory index which is related to $\boldsymbol{\beta}$ by

$$\varepsilon = \frac{1}{2\pi} \ln\left(\frac{1-\beta}{1+\beta} \right), \quad \beta = \left[-\frac{1}{2} tr\left(\boldsymbol{\beta}^2 \right) \right]^{1/2}. \tag{B3}$$

The real matrix function $\mathbf{Y}[\eta(z)]$ is explicitly defined in terms of $\boldsymbol{\beta}$ by Qu and Li [31] as

$$\mathbf{Y}\left[\eta(z) \right] \equiv \mathbf{I} + \frac{i}{2\beta} \left[\eta(z) - \bar{\eta}(z) \right] \boldsymbol{\beta} + \frac{1}{\beta^2} \left\{ 1 - \frac{1}{2} \left[\eta(z) + \bar{\eta}(z) \right] \right\} \boldsymbol{\beta}^2, \tag{B4}$$

where $\eta(z)$ is an arbitrary function of z. The matrix function $\mathbf{Y}[\eta(z)]$ plays an important role in representing the oscillatory fields near the crack tip. Certain properties of the matrix function $\mathbf{Y}[\eta(z)]$ are used for various derivations in this paper, and they are summarised as follows [31, 35]:

$$\mathbf{Y}\left[\eta_1(z)\right]\mathbf{Y}\left[\eta_2(z)\right] = \mathbf{Y}\left[\eta_1(z)\eta_2(z)\right], \tag{B5a}$$

$$\mathbf{Y}\left[\eta(\overline{z})\right] = \overline{\mathbf{Y}\left[\eta(z)\right]}, \tag{B5b}$$

$$\mathbf{U}\mathbf{Y}^T\left[\eta(\overline{z})\right]\mathbf{U}^{-1} = \mathbf{Y}\left[\overline{\eta}(z)\right], \tag{B5c}$$

$$\mathbf{Y}\left[\overline{\xi}(x_1 e^{i\pi})\right]\left(\mathbf{I} + i\boldsymbol{\beta}\right)^{-1} = \mathbf{Y}\left[x_1^{i\varepsilon}\cosh\pi\varepsilon\right], \tag{B5d}$$

$$\left(\mathbf{I} + i\boldsymbol{\beta}\right)\mathbf{Y}\left[\xi(x_1 e^{i\pi})\right] = \left(\mathbf{I} - i\boldsymbol{\beta}\right)\overline{\mathbf{Y}\left[\xi(x_1 e^{-i\pi})\right]}, \tag{B5e}$$

where η denotes an arbitrary function while ξ indicates the function $\xi(z) = z^{-i\varepsilon}$.

Appendix C: Orthogonalisation of the interaction J integral and orthogonal polynomials

In order to orthogonalise the interaction J integral of equation (8), the matrix function $\mathbf{Y}[\xi(z)]$ for $\xi(z)=z^{-i\varepsilon}$ should be diagonalised. From the definition of $\mathbf{Y}[\xi(z)]$ in equation (B4) and the property of a Hermitian matrix, as prepared by Beom and Atluri [35], the matrix function $\mathbf{Y}[\xi(z)]$ can be diagonalised as:

$$\mathbf{Y}\left[\xi(z)\right]=\bar{\mathbf{V}}^{-T}\tilde{\mathbf{\Lambda}}\left[\xi(z)\right]\bar{\mathbf{V}}^{T} \quad \text{or} \quad \mathbf{U}^{-1}\mathbf{Y}\left[\xi(z)\right]=\mathbf{V}\tilde{\mathbf{\Lambda}}\left[\xi(z)\right]\bar{\mathbf{V}}^{T}, \tag{C1}$$

in which $\tilde{\mathbf{\Lambda}}\left[\xi(z)\right]=diag\left[\xi(z),\bar{\xi}(z),1\right]$ and $\mathbf{V}\equiv\left(\mathbf{v}_1,\mathbf{v}_2,\mathbf{v}_3\right)$, where $\mathbf{v}_1$, $\mathbf{v}_2(=\bar{\mathbf{v}}_1)$, and $\mathbf{v}_3(=\bar{\mathbf{v}}_3)$ are eigenvectors corresponding to the eigenpairs $\left(-\varepsilon,\mathbf{v}_1\right)$, $\left(\varepsilon,\mathbf{v}_2\right)$, and $\left(0,\mathbf{v}_3\right)$ of $\left(\bar{\mathbf{M}}_{<1>}^{-1}+\mathbf{M}_{<2>}^{-1}\right)\left(\mathbf{M}_{<1>}^{-1}+\bar{\mathbf{M}}_{<2>}^{-1}\right)^{-1}\mathbf{v}=e^{2\pi\varepsilon}\mathbf{v}$. Therefore, by using the relation (C1), the interaction integral in equation (8) is rewritten as:

$$\begin{aligned}
J_{\Gamma_\varepsilon}^{\text{int}}[S,\hat{S}]&=\int_{-c}^{c}\sqrt{c^2-x_1^2}\left\{\mathbf{g}_0^T(x_1)\tilde{\mathbf{\Lambda}}\left[\xi_c(x_1)\right]\hat{\mathbf{h}}_0(x_1)+\hat{\mathbf{g}}_0^T(x_1)\tilde{\mathbf{\Lambda}}\left[\xi_c(x_1)\right]\mathbf{h}_0(x_1)\right\}dx_1\\
&\quad+4\int_{-c}^{c}\sqrt{c^2-x_1^2}\left[\mathbf{q}^T(x_1)\left(\mathbf{L}_{<1>}+\mathbf{L}_{<2>}\right)^{-1}\hat{\mathbf{r}}(x_1)+\hat{\mathbf{q}}^T(x_1)\left(\mathbf{L}_{<1>}+\mathbf{L}_{<2>}\right)^{-1}\mathbf{r}(x_1)\right]dx_1\\
&=c\int_{-1}^{1}\left[\mathbf{g}_0^T(cs)\tilde{\boldsymbol{\omega}}(s)\hat{\mathbf{h}}_0(cs)+\hat{\mathbf{g}}_0^T(cs)\tilde{\boldsymbol{\omega}}(s)\mathbf{h}_0(cs)\right]ds\\
&\quad+4c\int_{-1}^{1}\sqrt{1-s^2}\left[\mathbf{q}^T(cs)\left(\mathbf{L}_{<1>}+\mathbf{L}_{<2>}\right)^{-1}\hat{\mathbf{r}}(cs)+\hat{\mathbf{q}}^T(cs)\left(\mathbf{L}_{<1>}+\mathbf{L}_{<2>}\right)^{-1}\mathbf{r}(cs)\right]ds,
\end{aligned} \tag{C2}$$

where $\mathbf{g}_0(x_1)=\mathbf{V}^T\mathbf{g}(x_1)$, $\xi_c(x_1)=\left[(c-x_1)/(c+x_1)\right]^{-i\varepsilon}$, $\mathbf{h}_0(x_1)=\bar{\mathbf{V}}^T\mathbf{Y}\left[\cosh\pi\varepsilon\right]\mathbf{h}(x_1)$, and $s=x_1/c$. The weight function $\tilde{\boldsymbol{\omega}}(s)$ is a diagonal matrix with the components of $\omega_j(s)\delta_{jk}$ and

$$\omega_j(s)=(1-s)^{a_j}(1+s)^{\bar{a}_j} \quad \left(j=1,2,3\right), \tag{C3}$$

in which the exponents are written in terms of ε as $a_1=1/2-i\varepsilon$, $a_2=1/2+i\varepsilon$, and $a_3=1/2$. Then, the analytic functions $\mathbf{g}_0(cs)$ and $\mathbf{h}_0(cs)$ can be expanded in terms of Jacobi polynomials, denoted as $P_n^{(a,b)}(s)$, which are orthogonal at the interval $[-1,1]$ with a weight function of $\omega(s)$ as

$$\int_{-1}^{1} \frac{P_m^{(a,b)}(s)}{\theta_m^{(a,b)}} \frac{P_n^{(a,b)}(s)}{\theta_n^{(a,b)}} \omega(s) ds = \frac{\pi}{2} \delta_{mn} , \tag{C4}$$

where $\theta_n^{(a,b)} = \sqrt{2^{a+b+2}\Gamma(n+a+1)\Gamma(n+b+1) \big/ \left[\pi(2n+a+b+1)\Gamma(n+1)\Gamma(n+a+b+1)\right]}$ and $\Gamma(z)$ is a gamma function. The first two terms and the recurrence relations of the Jacobi polynomials are given by

$$\begin{aligned} & P_0^{(a,b)}(s) = 1, \\ & P_1^{(a,b)}(s) = \frac{a-b}{2} + \left(1 + \frac{a+b}{2}\right)s, \\ & \frac{2(n+1)(n+a+b+1)}{(2n+a+b+1)(2n+a+b+2)} P_{n+1}^{(a,b)}(s) \\ & \quad = \left[\frac{(a^2-b^2)}{(2n+a+b)(2n+a+b+2)} + s \right] P_n^{(a,b)}(s) - \frac{2(n+a)(n+b)}{(2n+a+b)(2n+a+b+1)} P_{n-1}^{(a,b)}(s). \end{aligned} \tag{C5}$$

On the other hand, $\mathbf{q}(cs)$ and $\mathbf{r}(cs)$ may be expanded in terms of the Chebyshev polynomials of the second kind, denoted by $U_n(s)$, which are a special case of the Jacobi polynomials $P_n^{(a,b)}(s)$ with $a = b = 1/2$.

References

[1] R.E. Peierls, Proc. Phys. Soc. **52** 34 (1940).

[2] F.R.N. Nabarro, Proc. Phys. Soc. **59** 256 (1947).

[3] G.I. Barrenblatt, Advances in Applied Mechanics **7** 55 (1962).

[4] J.R. Rice, J. Mech. Phys. Solids **40** 239 (1992).

[5] Y. Sun, G.E. Beltz, and J.R. Rice, Mater. Sci. Eng. **A170** 67 (1993).

[6] Y. Sun and G.E. Beltz, J. Mech. Phys. Solids **42** 1905 (1994).

[7] R. Miller and R. Phillips, Phil. Mag. **A73** 803 (1996).

[8] K.D. Da Silva, G.E. Beltz, and A. Machova, Scripta Mater. **49** 1163 (2003).

[9] S.M. Foiles, M.I. Baskes, and M.S. Daw, Phys. Rev. B **33** 7983 (1986).

[10] F.H.K. Chen and R.T. Shield, ZAMP J. Appl. Math. Phys. **28** 1 (1977).

[11] S. Hong and K.-S. Kim, J. Mech. Phys. Solids **51** 1267 (2003).

[12] R.G. Hoagland, M.S. Daw, S.M. Foiles, and M.I. Baskes, J. Mater. Res. **5** 313 (1990).

[13] R.G. Hoagland, M.S. Daw, and J.P. Hirth, J. Mater. Res. **6** 2565 (1991).

[14] P. Gumbsch, J. Mater. Res. **10** 2897 (1995).

[15] P. Gumbsch, and G.E. Beltz, Modelling Simul. Mater. Sci. Eng. **3** 597 (1995).

[16] R.G. Hoagland, Phil. Mag. **A76** 543 (1997).

[17] F. Cleri, S.R. Phillpot, D. Wolf, and S. Yip, J. Am. Ceram. Soc. **81** 501 (1998).

[18] J. Schiotz and A.E. Carlsson, Phil. Mag. A **80** 69 (2000).

[19] U.V. Waghmare, E. Kaxiras, and M.S. Duesbery, Physica Status Solidi B **217** 545 (2000).

[20] J.E. Sinclair and B.R. Lawn, Proc. Roy. Soc. Lon. A **329** 83 (1972).

[21] Y.W. Zhang, T.C. Wang, and H.Q. Tang, Scr. Metall. Mater. **33** 267 (1995).

[22] L. Hua, H. Rafii-Tabar, and M. Cross, Phil. Mag. Lett. **75** 237 (1997).

[23] R. Miller, M. Ortiz, R. Phillips, V. Shenoy, and E.B. Tadmor, Eng. Fract. Mech. **61** 427 (1998).

[24] J.R. Rice and J.-S. Wang, Materials Science and Engineering **A107** 23 (1989).

[25] C.H. Wu and M.L. Wang, J. Mech. Phys. Solids **48** 2283 (2000).

[26] N.I. Muskhelishvili, *Some basic problems of the mathematical theory of elasticity* (Groningen, Noordhoff, 1953).

[27] J.D. Eshelby, W.T. Read, and W. Shockley, Acta Metall. **1** 251 (1953).

[28] A.N. Stroh, Phil. Mag. **3** 625 (1958).

[29] S.G. Lekhnitskii, *Theory of elasticity of an anisotropic body* (Holden-Day, Inc., San Francisco, 1963).

[30] Z. Suo, Proc. R. Soc. Lond. **A427** 331 (1990).

[31] J. Qu and Q. Li, J. Elasticity **26** 169 (1991).

[32] H.G. Beom and S.N. Atluri, Computational Mechanics **16** 106 (1995).

[33] T.C.T. Ting, Int. J. Solids Structures **32** 483 (1995).

[34] J. Dundurs, ASME J. Appl. Mech. **36** 650 (1969).

[35] H.G. Beom and S.N. Atluri, Int. J. Fract. **75** 163 (1996).

[36] J.R. Rice, ASME J. Appl. Mech. **35** 379 (1968).

[37] S.T. Choi, H. Shin, and Y.Y Earmme, Int. J. Solids Structures **40** 1411 (2003).

[38] G.F. Voronoi, J. Reine Angew. Math. **134** 198 (1908).

[39] F.Z. Li, C.F. Shih, and A. Needleman, Eng. Fract. Mech. **21** 405 (1985).

[40] J.H. Rose, J. Ferrante, and J.R. Smith, Phys. Rev. Lett. **47** 675 (1981).

[41] V. Vitek, Phil. Mag. **18** 773 (1968).

[42] A.A. Griffith, Philosophical Transactions A **221** 163 (1920).

[43] T.C.T. Ting, *Anisotropic Elasticity: Theory and Applications* (Oxford University Press, New York, 1996).

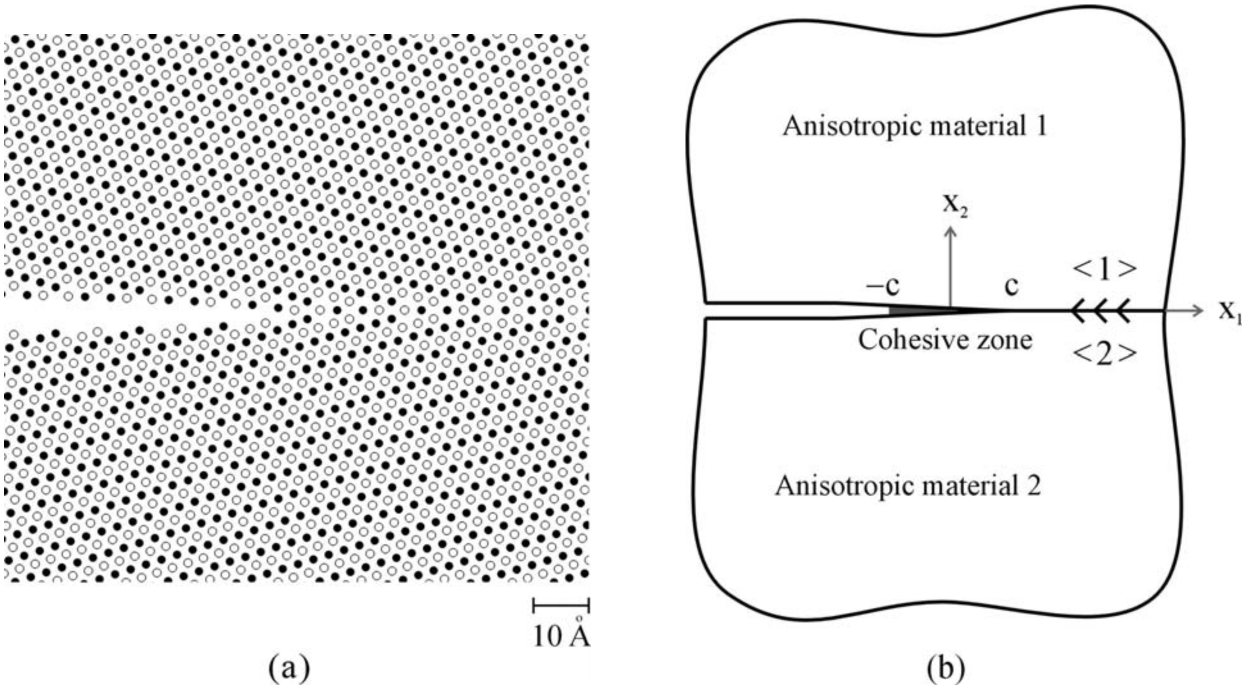

Figure 1. Deformation field near a crack with a cohesive zone size of 2c on an interface between two anisotropic solids: (a) an atomistic deformation field of decohesion along the $\Sigma 27$ grain boundary simulated using the EAM, and (b) a mathematical field model of decohesion interaction with atomistic deformation field. The black and white circles in (a) represent atoms in two alternating $(\bar{1}10)$ atomic planes.

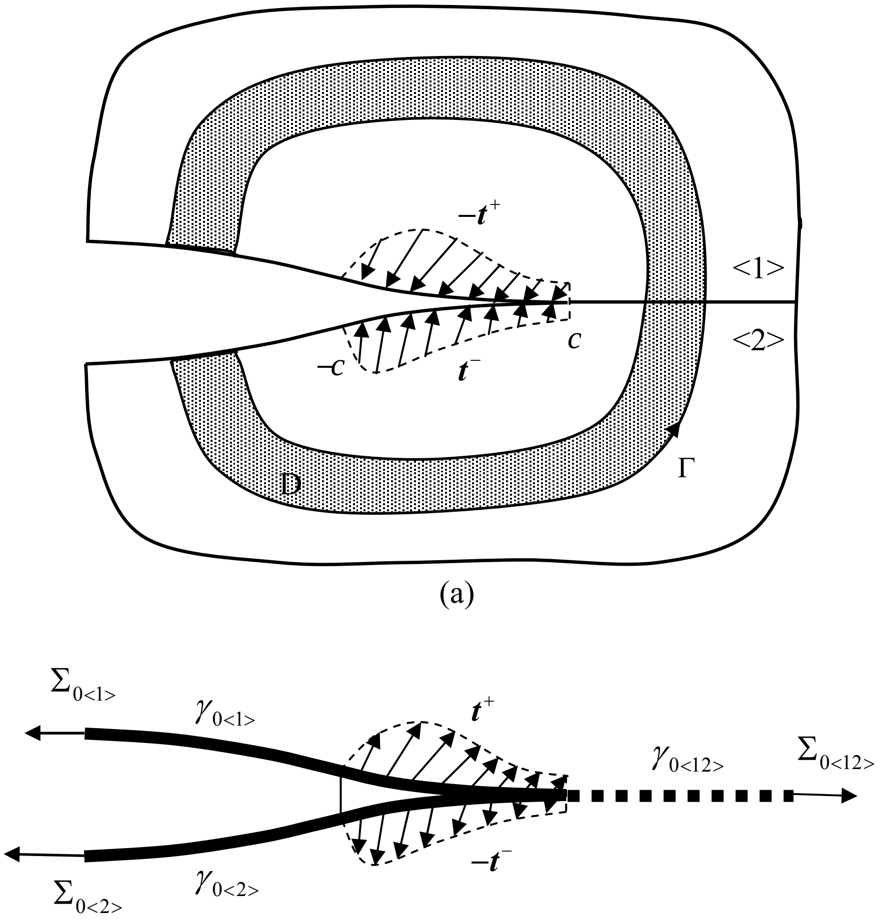

(a)

(b)

Figure 2. Schematics of the configurational force balance in a nano-scale crack-tip cohesive zone model: (a) a diagram of the bulk region, illustrating the domain of the interaction J integrals encompassing a cohesive crack tip, and (b) a diagram of the surface-interface region showing the configurational force balance in the region.

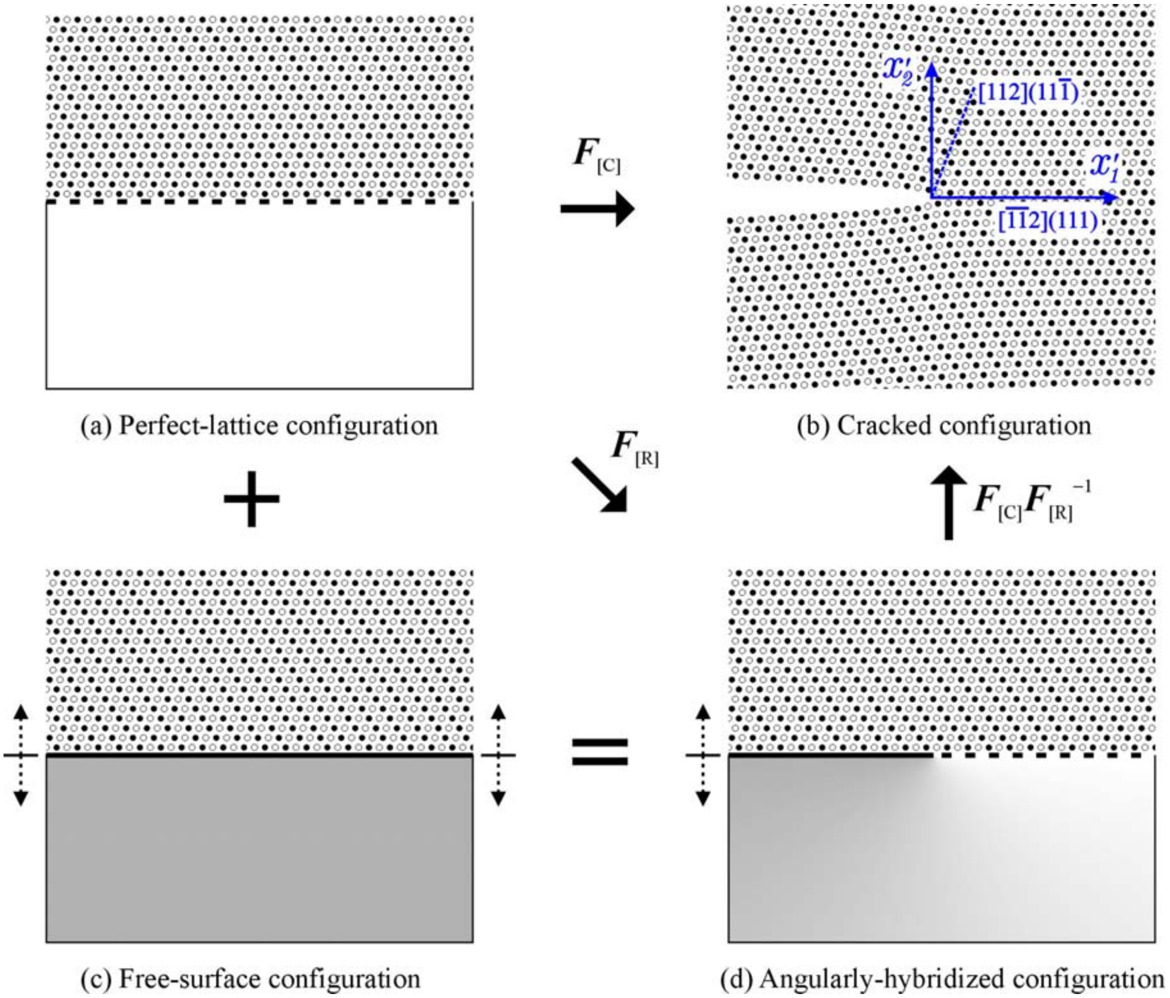

Figure 3. The kinematics of an atomistic deformation near a crack tip, expressed with combinations of the deformation gradients $\boldsymbol{F}_{[C]}$ and $\boldsymbol{F}_{[R]}$. Three nominal stress-free reference configurations are shown for (a) bulk deformation, (c) deformation near a free surface, and (d) deformation near a crack tip, while an equilibrium configuration is shown in (b) for an atomistic deformation field near a crack tip opening along a $[\bar{1}\bar{1}2]$ direction in a (111) plane in gold. The lower halves of (a), (c), and (d) depict continuum representations.

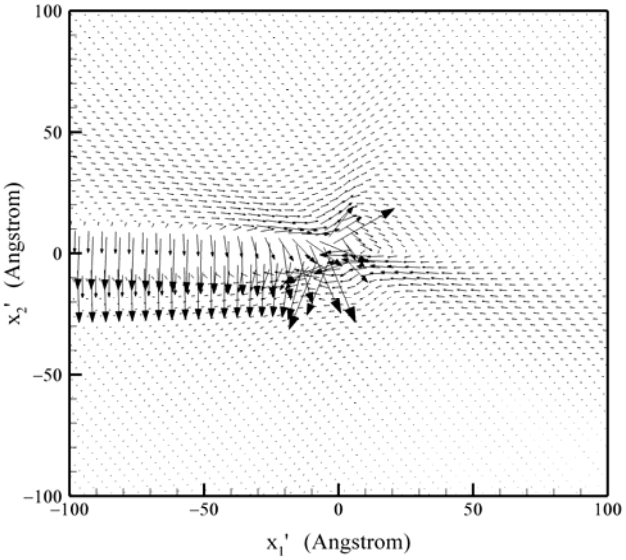

(a)

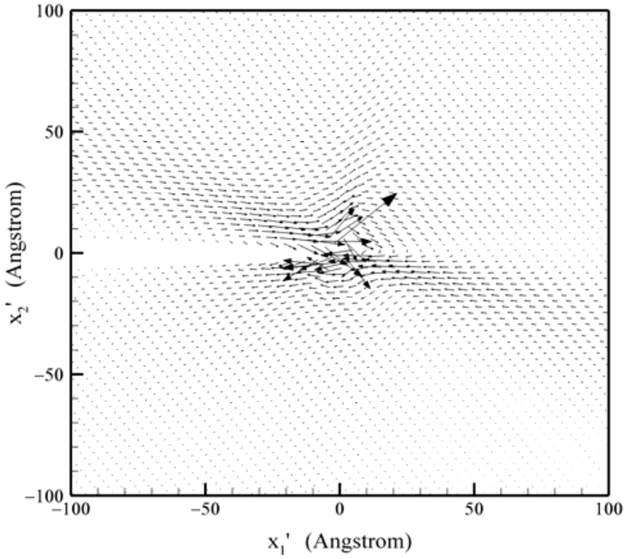

(b)

Figure 4. Vector plots of the displacement gradient in x_2' direction, $\left(\partial u_1 / \partial x_2', \partial u_2 / \partial x_2'\right)$, at each atomic site for the atomistic deformation of figure 3(b). Displacements are measured with respect to (a) a perfect configuration and (b) the hybrid configuration of figure 3(d).

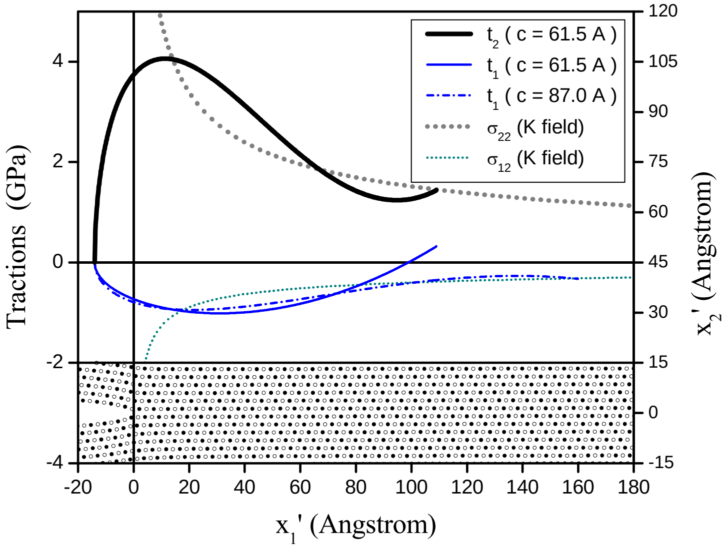

Figure 5(a). Cohesive zone traction distributions of the near-crack-tip field. The end positions of the cohesive zone are chosen as $x_1^a = -14$ Å and $x_1^b = 109$ Å ($c = 61.5$ Å), for which traction t_2 matches well with the applied K -field. Traction t_1 matches better with the applied K -field for an independent choice, for t_1 only, of $x_1^a = -14$ Å and $x_1^b = 160$ Å ($c = 87.0$ Å) (dash-dot line). The atomic positions near the crack tip simulated by the EAM, the same as those in figure 3(b), are also shown for comparison.

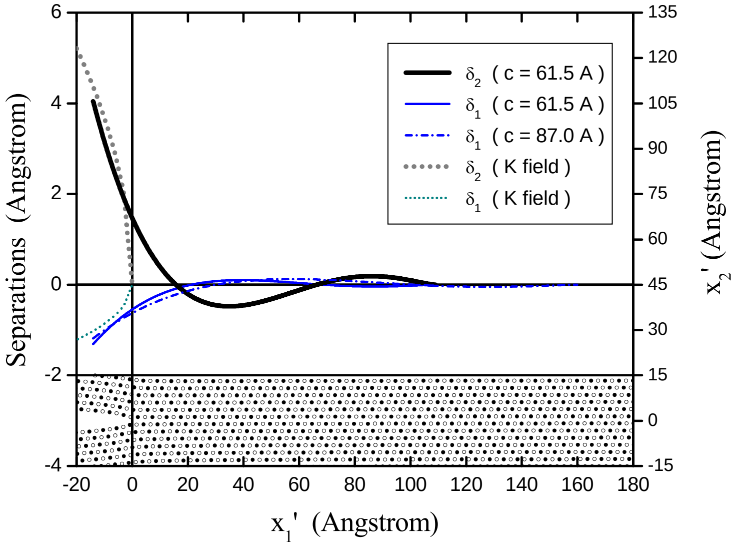

Figure 5(b). Cohesive zone separations for $x_1^a = -14$ Å and $x_1^b = 109$ Å ($c = 61.5$ Å). Another measure (dash-dot line) of the shear separation is also plotted for the choice of $x_1^a = -14$ Å and $x_1^b = 160$ Å ($c = 87.0$ Å). The atomic positions near the crack tip simulated by the EAM, the same as those in figure 3(b), are also shown for comparison.

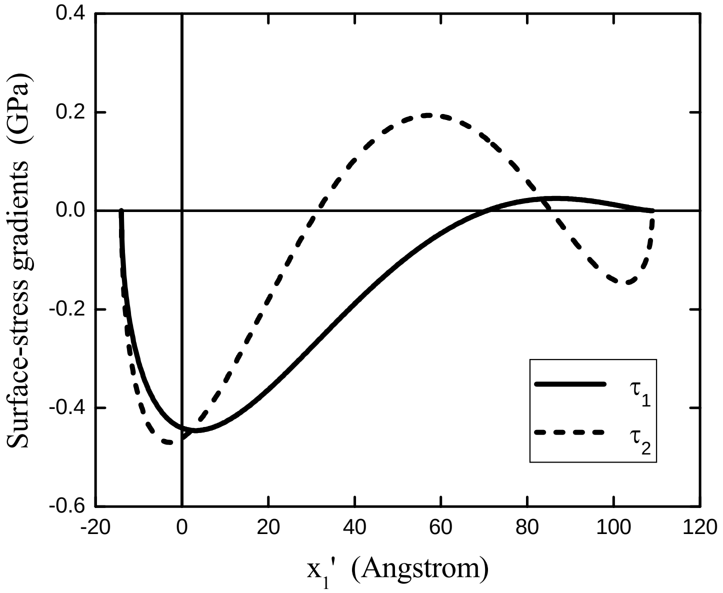

Figure 6(a). Surface stress gradients along the cohesive zone.

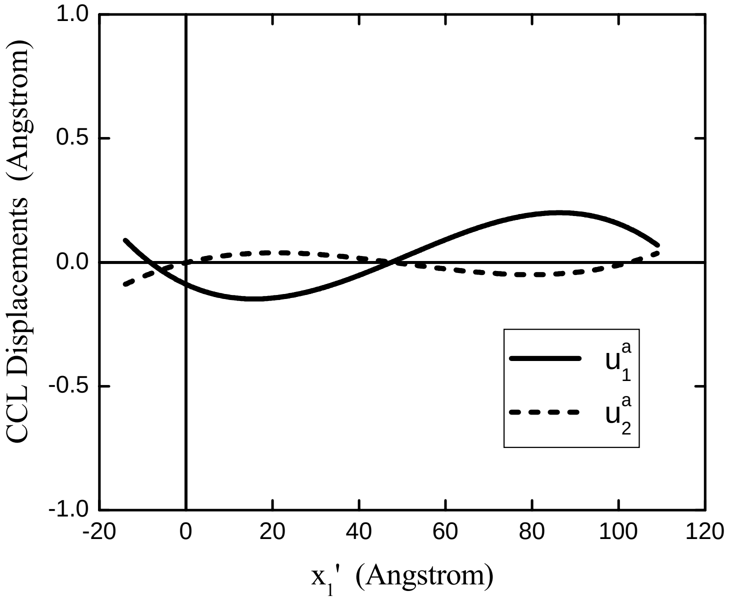

Figure 6(b). Cohesive-zone centre line (CCL) displacements at the cohesive zone.

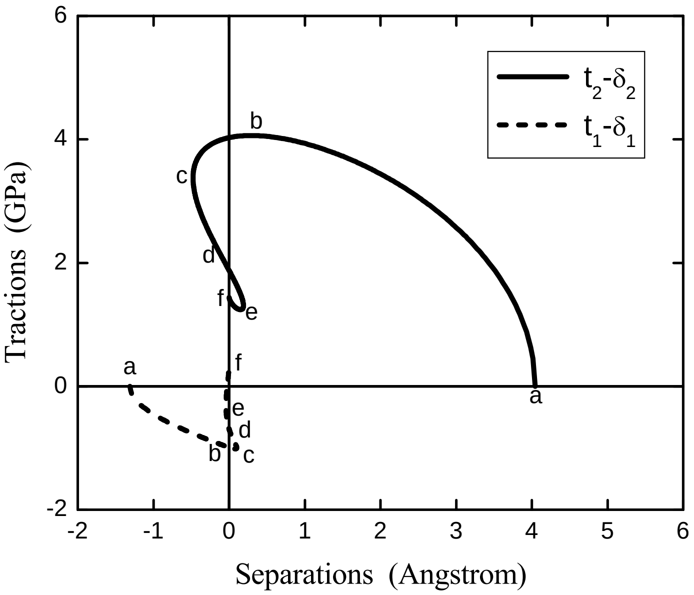

Figure 6(c). Cohesive zone traction-separation relations.

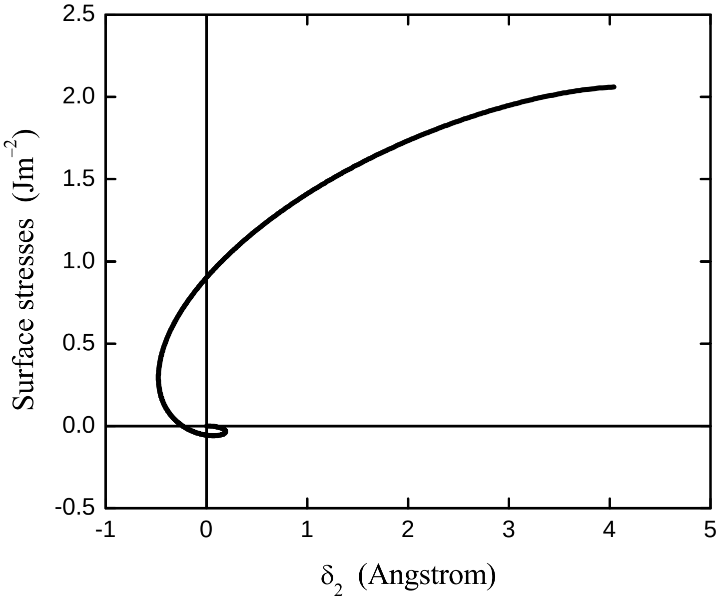

Figure 6(d). Cohesive zone surface stresses.

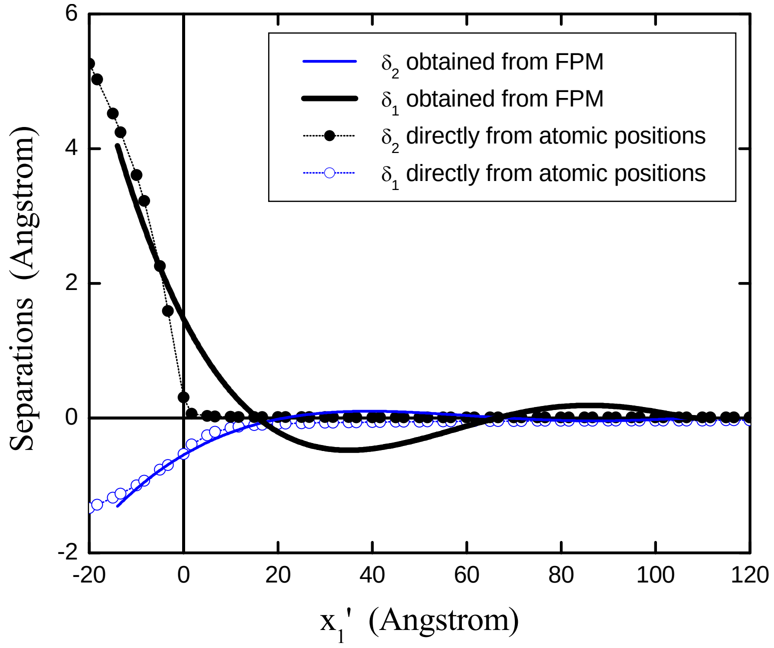

Figure 7(a). Cohesive zone separations. The solid lines represent the separation profiles obtained by the FPM along the crack plane. The open and solid circles indicate shear and normal atomic-site separations, respectively, between adjacent atomic planes across the cohesive zone.

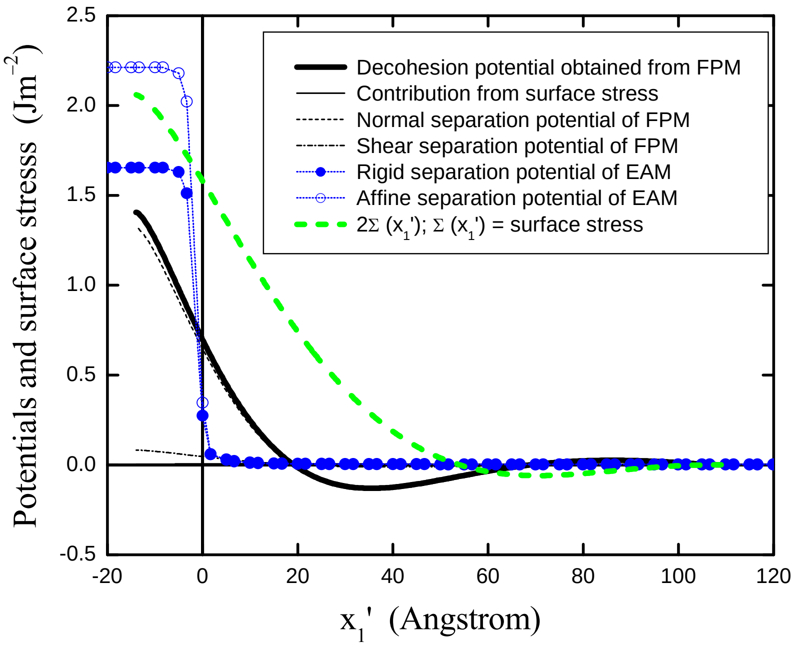

Figure 7(b). Field-projected separation potentials and surface stress are plotted with the rigid and affine separation potentials of EAM, shown as solid and open circles, respectively.

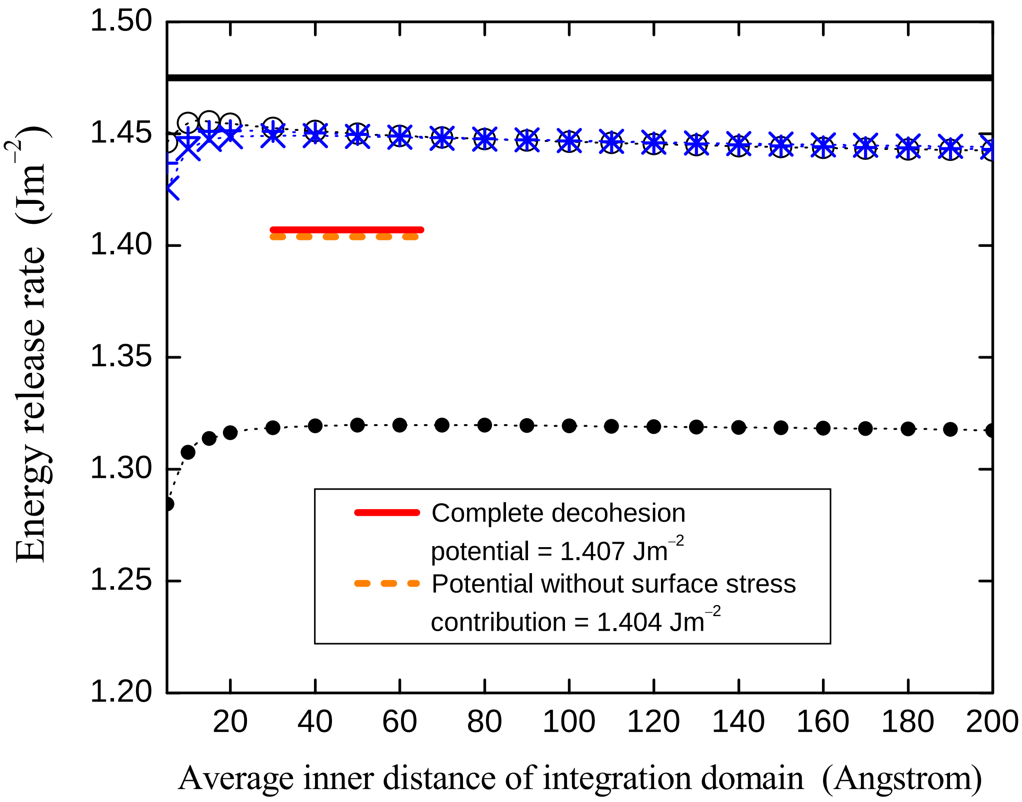

Figure 8. Energy release rates evaluated by various conservation integrals with different integral domains. The thick solid line is the applied nominal energy release rate, 1.475 Jm^{-2}. The evaluation of J integrals with $\boldsymbol{F}_{[H]}$ is shown by open circles; J integrals with $\boldsymbol{F}_{[C]}$ by solid circles; interaction J integrals with $\boldsymbol{F}_{[H]}$ by '+' marks; and interaction J integrals with $\boldsymbol{F}_{[C]}$ by '×' marks.

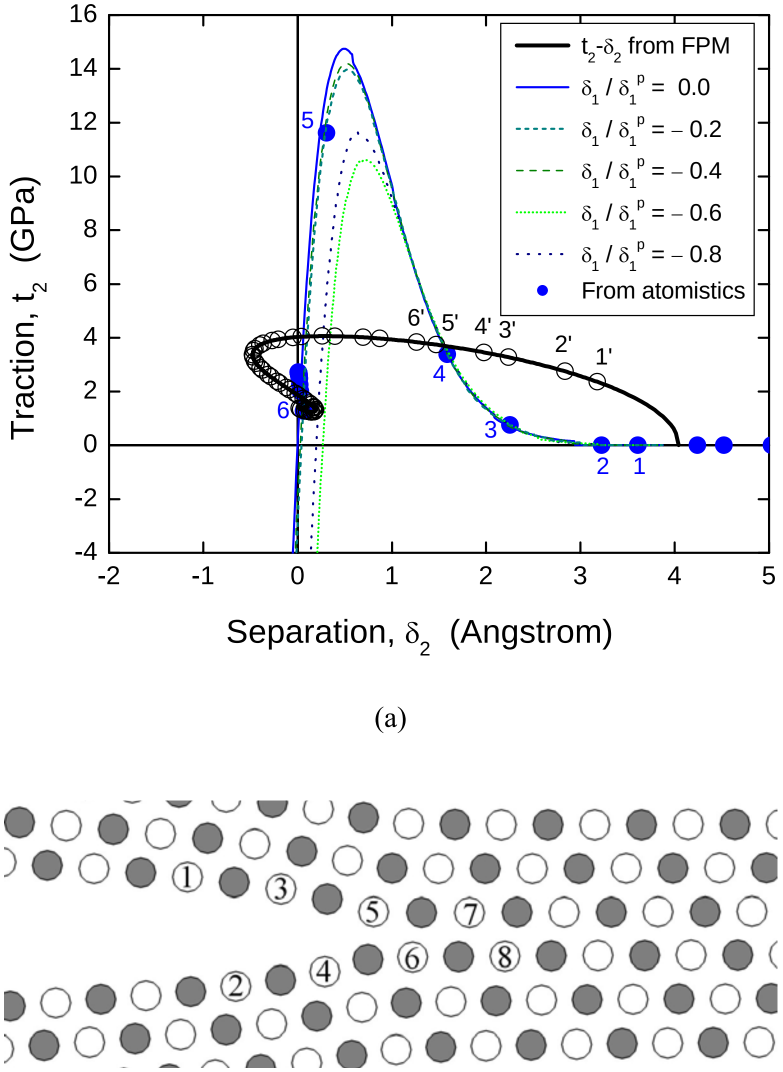

(a)

(b)

Figure 9. (a) Comparison between two nominal states of cohesive zone separation measured by the RSP method (solid circles) and the FPM (open circles) at cohesive zone atomic sites. (b) Atomistic deformation configuration near the crack tip and the cohesive zone atomic sites.